Simulation and optimization of nanostructured silicon photodiode

Juha Heinonen

School of Electrical Engineering

Thesis submitted for examination for the degree of Master of Science in Technology.

Espoo 11.4.2016

Thesis supervisor:

Prof. Hele Savin

Thesis advisor:

D.Sc. (Tech.) Mikko Juntunen

Aalto University
School of Electrical Engineering

AALTO UNIVERSITY
SCHOOL OF ELECTRICAL ENGINEERING

ABSTRACT OF THE
MASTER'S THESIS

Author: Juha Heinonen

Title: Simulation and optimization of nanostructured silicon photodiode

Date: 11.4.2016 Language: English Number of pages: 8+55

Department of Micro and Nanosciences

Professorship: Semiconductor technology

Supervisor: Prof. Hele Savin

Advisor: D.Sc. (Tech.) Mikko Juntunen

In this work, a new type of silicon photodiode concept was investigated with the help of device simulations performed with Silvaco Atlas. The operation of the photodiode is based on inversion layer which is induced by a negatively charged aluminum oxide film. Photogenerated current is collected with this induced junction which eliminates the need for traditional doped pn-junction and results into minimal recombination losses. Optical reflections from the device surface are almost completely eliminated by covering the surface with black silicon. Combination of these optical and electrical properties results into a photodiode with nearly ideal performance.
The simulations were used to investigate how different parameters affect to the device operation. The most important goal was to find a way to decrease the magnitude of leakage current to a more reasonable level. Based on the gained knowledge, a new version of the photodiode was designed. The main difference in the new design is the addition of a guard ring structure which, according to simulations, should decrease leakage current by approximately five orders of magnitude.

Keywords: Silicon photodiode, Nanostructures, Simulation, Silvaco Atlas

AALTO-YLIOPISTO
SÄHKÖTEKNIIKAN KORKEAKOULU

DIPLOMITYÖN
TIIVISTELMÄ

Tekijä: Juha Heinonen

Työn nimi: Nanokuvioidun piifotodiodin simulointi ja optimointi

Päivämäärä: 11.4.2016 Kieli: Englanti Sivumäärä: 8+55

Mikro- ja nanotekniikan laitos

Professuuri: Puolijohdeteknologia

Työn valvoja: Prof. Hele Savin

Työn ohjaaja: TkT Mikko Juntunen

Tässä työssä tutkittiin uudentyyppistä piifotodiodikonseptia Silvaco Atlas-nimisellä laitesimulaattorilla. Kyseisen fotodiodin toiminta perustuu negatiivisesti varatun alumiinioksidikalvon indusoimaan inversiokerrokseen, jota käytetään absorboidun valon tuottaman virran keräämiseen. Tällä tavoin päästään eroon perinteisesti käytetystä seostamalla toteutetusta pn-liitoksesta ja saadaan minimoitua rekombinaatiohäviöt. Optiset heijastukset laitteen pinnasta on saatu eliminoitua lähes kokonaan peittämällä fotodiodin pinta mustalla piillä. Nämä optiset ja sähköiset ominaisuudet yhdistämällä saavutetaan lähes ideaalisesti käyttäytyvä fotodiodi.
Simulaatioiden avulla tutkittiin sitä miten eri parametrit vaikuttavat laitteen toimintaan. Tärkeimpänä tavoitteena oli selvittää miten vuotovirtaa voisi pienentää nykyisestä tasosta. Simulaatiotuloksista opittujen seikkojen perusteella fotodiodista suunniteltiin uusi versio. Suurin muutos laitteen rakenteeseen on suojarenkaan lisääminen, jonka simulaatioiden mukaan pitäisi pienentää vuotovirtaa noin viisi dekadia.

Avainsanat: Piifotodiodi, Nanorakenteet, Simulaatio, Silvaco Atlas

Preface

This thesis is based on the work I did in the Electron Physics group at the Aalto University Department of Micro and Nanosciences between the fall of 2015 and spring of 2016. Funding for the research came from TEKES project RADI-2014.

First of all, I would like to thank my supervisor Hele Savin for the opportunity to work in the Electron Physics group and for the guidance throughout the process of making this thesis. I also want to thank my advisor Mikko Juntunen. His advice and expertise on photodiodes have been invaluable resources and without them the outcome of this work would not have been this good. All other members of the research group also deserve my deepest gratitude for all their help and for making these past months a much more fun experience. Finally, I would like to thank my family and friends for their support during all the good and bad days.

Otaniemi, 11.4.2016

Juha Heinonen

Contents

Abstract ii

Abstract (in Finnish) iii

Preface iv

Contents v

Symbols and abbreviations vi

1 Introduction 1

2 Theory 3
2.1 Photodiode . . . 3
2.2 Photogeneration and recombination . . . 8
2.2.1 Shockley-Read-Hall recombination . . . 11
2.2.2 Auger recombination . . . 11
2.2.3 Surface recombination . . . 13
2.2.4 Surface passivation . . . 13
2.2.5 Secondary ionization . . . 14
2.3 Oxide charge . . . 14
2.4 Induced junction photodiode . . . 15
2.5 Black silicon . . . 18

3 Methods 22
3.1 Device fabrication . . . 22
3.2 Simulations . . . 24

4 Results 29
4.1 Black silicon simulation results . . . 29
4.2 Planar photodetector simulation results . . . 31
4.2.1 Inversion and depletion layer . . . 31
4.2.2 Inversion layer sheet resistance . . . 35
4.2.3 Spectral response . . . 38
4.2.4 Effects of contact size and doping profile . . . 43
4.2.5 Effects of guard ring . . . 45

5 Conclusions 48

References 50

Symbols and abbreviations

Symbols

A	surface area
a	absorption
C	capacitance
c_n	Auger coefficient for electrons
c_p	Auger coefficient for holes
D_p	photodiode
E_c	conduction band edge energy level
E_F	Fermi level
E_g	bandgap energy
E_i	intrinsic Fermi level
E_p	photon energy
E_t	trap state energy
E_v	valence band edge energy level
g_{eeh}	Auger coefficient enhancement factor for electrons
g_{ehh}	Auger coefficient enhancement factor for holes
I	current
I_{dark}	dark current
I_p	photogenerated current
k_B	Boltzmann constant $\approx 1.381 \times 10^{-23}$ [J/K]
n	electron concentration
N_a	acceptor concentration
N_b	bulk doping concentration
N_d	donor concentration
n_i	intrinsic carrier concentration
N_{net}	net doping concentration
Δn	injected excess carrier density
p	hole concentration
P_i	light intensity of beam i
q	elementary charge $\approx 1.602 \times 10^{-19}$ [C]
Q_f	fixed oxide charge density
r	reflectance
R	resistance
R_{sh}	sheet resistance
S_{CN}	surface recombination velocity of electrons on silicon-aluminum interface
S_{CP}	surface recombination velocity of holes on silicon-aluminum interface
S_{eff}	effective surface recombination velocity
S_{EN}	surface recombination velocity of electrons on device edges
S_{EP}	surface recombination velocity of holes on device edges
S_N	surface recombination velocity of electrons on silicon-aluminum oxide interface
S_P	surface recombination velocity of holes on silicon-aluminum oxide interface
T	temperature

t	transmittance
T_L	lattice temperature
V	voltage
V_b	bias voltage
V_{out}	output voltage
w	wafer thickness
W_{dep}	width of depletion layer
W_{max}	depletion region maximum depth
x_j	depth of inversion layer
x_n	width of the depletion layer on the n side of pn-junction
x_p	width of the depletion layer on the p side of pn-junction
y_p	doping concentration peak distance from surface
ϵ_s	silicon permittivity
μ_p	hole mobility
τ_{Auger}	carrier lifetime determined by Auger recombination
$\tau_{Auger,hi}$	Auger recombination lifetime in high-injection condition
$\tau_{Auger,li}$	Auger recombination lifetime in low-injection condition
τ_{bulk}	bulk lifetime
τ_{eff}	measured effective lifetime
τ_n	lifetime of electrons determined by Shockley-Read-Hall recombination
τ_{n0}	electron capture time constant
τ_p	lifetime of holes determined by Shockley-Read-Hall recombination
τ_{p0}	hole capture time constant
τ_{rad}	carrier lifetime determined by radiative recombination
τ_{SRH}	carrier lifetime determined by Shockley-Read-Hall recombination
τ_{surf}	carrier lifetime on surface
τ_{total}	total carrier lifetime
ϕ_{bi}	built-in potential of a pn-junction
ϕ_f	Fermi potential
ϕ_s	surface potential

Abbreviations

2D	two-dimensional
Al_2O_3	aluminum oxide
ALD	atomic layer deposition
ARC	anti-reflective coating
b-Si	black silicon
CV	capacitance-voltage
CT	computed tomography
DRIE	deep reactive ion etching
EHP	electron-hole pair
EQE	external quantum efficiency
ICP-RIE	inductive coupled plasma - reactive ion etching
IQE	internal quantum efficiency

IR	infrared
IV	current-voltage
ppm	parts per million
PQED	predictable quantum efficient detector
SEM	scanning electron microscope
SiN_x	silicon nitride
SiO_2	silicon dioxide
SRH	Shockley-Read-Hall
SRV	surface recombination velocity

1 Introduction

Photodiode is a semiconductor device that converts light into electrical signal through the photoelectric effect. In ideal photodiode every incoming photon is converted and thus the magnitude of the electrical signal depends linearly on the number of photons i.e. the intensity of the incident light. Unfortunately, even the best commercially available photodiodes are far from this level of performance. They suffer from severe optical losses and a comparable performance can be achieved only within a very narrow wavelength range by utilizing a carefully optimized anti-reflective coating (ARC). Furthermore, damage inflicted during the fabrication process can cause losses via carrier recombination. The purpose of this thesis is to investigate a new photodiode concept that utilizes black silicon and induced junction to overcome these problems.

Silicon surface covered with nanostructures i.e. black silicon (b-Si), has been shown to eliminate reflections almost completely across the visible light spectrum [1]. This makes it a very attractive option for replacing the ARCs. Despite the huge potential, b-Si is currently rarely used in commercial devices. The reason has been the increased surface area which promotes surface recombination. Increased carrier losses due to surface recombination have been larger than the benefits gained from reduced reflectance and thus the overall performance has been worse than in planar devices. Recent advances in surface passivation of b-Si with aluminum oxide (Al_2O_3) grown with atomic layer deposition (ALD) [2, 3] have practically solved this problem and very promising results have been obtained with solar cells [4]. There is no reason why the same principle would not work in photodiodes and indeed, impressive results have been obtained in a study preceding this thesis [5].

Secret behind the impressive passivation performance of Al_2O_3 is the excellent conformality achieved with ALD. In addition, the high negative charge present in the film greatly enhances the passivating properties. In our photodiode concept, the charge also serves another purpose. It is used to induce a charge collecting pn-junction into high resistivity n-type silicon. In traditional photodiodes, the pn-junction is formed by adding dopant atoms into silicon. This method creates damage to the silicon lattice which increases recombination losses. In addition, the high dopant concentration promotes Auger recombination. Induced junction eliminates both of these problems and results into almost ideal charge collection performance. When combined with the optical properties of b-Si, almost ideal response can be achieved in the entire visible light range.

The concept of induced junction photodiode was first demonstrated by Hansen in 1978 [6]. He used p-type silicon substrate and positive charge present in silicon oxide to induce a pn-junction. More recently, induced junction photodiodes have been used in development of primary standard of optical power [7]. However, none of the induced junction photodiodes have gained much commercial interest. The industry standard is to use n-type substrate and thus the induced junction photodiodes based on p-type substrate have not been attractive options. Our concept utilizes n-type substrate which increases its commercial potential. One photodiode utilizing b-Si has also been reported before [8]. Laser processing is utilized to form the b-Si and

doped pn-junction. Our device is the first one that combines b-Si and an induced junction.

The near-ideal operation would bring benefits to numerous applications. Practically all devices where detection of light is needed could gain improvements one way or the other. Medical and security X-ray scanners [9], blood particle analyzers [10], and encoders [11] are just a few examples where the advantages of better photodiode performance would bring improvements. For example, X-ray scanners utilize scintillator to convert X-rays into light which is then measured with photodiodes [12]. Improved photodiode sensitivity would allow better resolution with the same amount of radiation than before. Alternatively, a smaller amount of radiation could be used to produce images with the same resolution than before. The first application for our photodiodes could be in computed tomography (CT) due to previous experience from the topic in our group [13].

The main goal of this work was to study the photodiode concept with the help of simulations and then improve the current design. Although performance is already very impressive, there are still many aspects that could be improved. Especially, the leakage current should be reduced because it is still large compared to commercial devices. Very impressive quantum efficiency of over 95 % across the visible wavelength range has been already measured. However, it is still a couple of percent below expected level. Therefore, room for improvement still exists. Another goal was to study inversion layer sheet resistance in Al_2O_3 coated b-Si. Currents in photodiodes are so small that the sheet resistance does not have a significant impact on the performance. In solar cells, the currents are larger and thus sheet resistance plays a much more important role. If the inversion layer sheet resistance is low enough, it should be possible to apply this concept also in solar cells.

Device simulations with Silvaco Atlas were performed to get an idea how different parameters affect the device operation. Several different aspects of b-Si and induced junction photodiodes were studied and the results were compared with other photodiodes and with measurement results form the first version of the device. Based on the findings, a new set of photomasks was designed and a new batch of photodiodes was fabricated with them.

This thesis is structured as follows. First, a brief introduction to the operation principle of photodiodes is given along with descriptions of the most essential phenomena related to our photodiode concept. Next, details and measurement results from the first batch of our devices are given followed by an introduction to the simulations. After that, simulation results are presented and discussed. In the end, a short summary of the entire thesis is given.

2 Theory

2.1 Photodiode

The basic idea of a photodiode is simple: electric field in a pn-junction is used to separate photogenerated charge carriers which are then collected with metal contacts. In order to design a photodiode, it is essential to truly understand the physics related to pn-junction. However, a detailed analysis is beyond the scope of this work and only a brief discussion about the most important principles is given. A more extensive description can be found in many semiconductor physics textbooks (e.g. [14, 15]).

When p-doped silicon is contacted with n-doped silicon, a pn-junction is formed. The n-type impurity atoms in silicon add free electrons and p-type impurity atoms create holes. Near the junction, these electrons and holes can diffuse to the other sides of the junction and recombine, leaving the original host atoms ionized. Consequently, these areas become depleted from charge carriers and the ionized atoms form an electric field across the depleted region. In the band diagram, shown in figure 1, this is seen as bending of the valence and conduction bands. The potential difference caused by the band bending is called built-in potential ϕ_{bi}. The magnitude of ϕ_{bi} is a function of carrier concentrations and thus it is a one common metric used to describe properties of pn-junctions. [14]

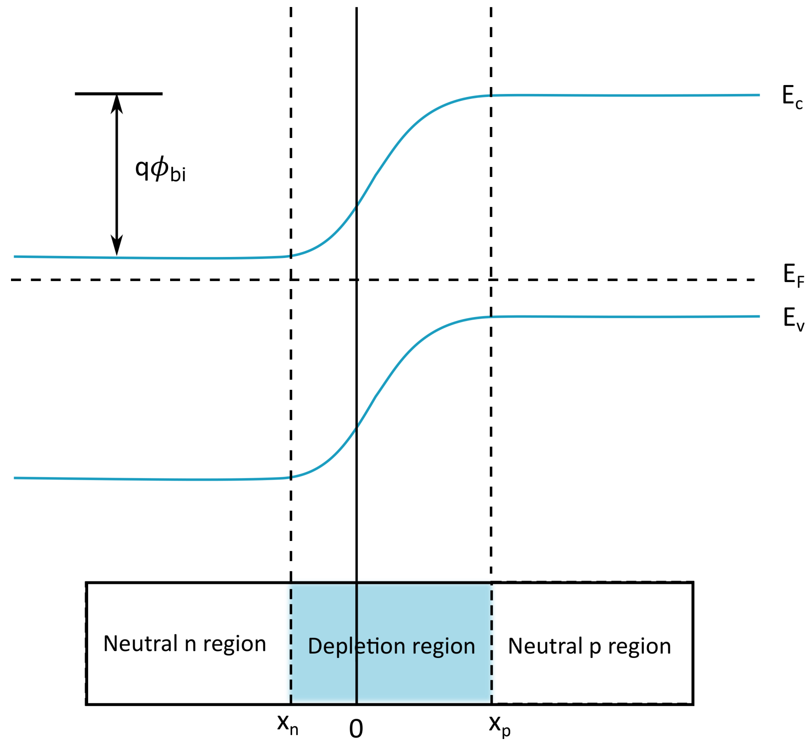

Figure 1: Band diagram of a pn-junction. x_n and x_p are the portions of depletion layer on the corresponding sides of the junction. E_c, E_F, and E_v are the conduction band, Fermi level, and valence band energy levels, respectively.

In photodiodes, electric field in the depletion region is used for current collection. Any electrons or holes generated by light in the depletion region get swept to the opposite sides of the junction which prevents them from recombining. Contacting different sides of the junction will result into a current flowing between the contacts. Magnitude of the current is related to the intensity of the light that created the carriers.

Width of the depletion layer is determined by the dopant atom concentrations, built-in potential and possible bias voltage. In general case the width can be calculated from [14]

$$W_{dep} = \sqrt{\frac{2\epsilon_s(\phi_{bi} + V_b)}{q}\left(\frac{1}{N_a} + \frac{1}{N_d}\right)} \tag{1}$$

where ϵ_s is the permittivity of silicon, ϕ_{bi} is the built-in potential, V_B is the bias voltage, q is the elementary charge, N_a is the acceptor concentration, and N_d is the donor concentration. However, often one of the sides has a considerably higher dopant concentration than the other. Then the majority of the depletion region is located in the side with lighter doping and the portion on the other side is negligibly small. In this case the previous equation can be simplified. If the p side is significantly more heavily doped the equation becomes

$$W_{dep} \approx |x_n| \approx \sqrt{\frac{2\epsilon_s(\phi_{bi} + V_b)}{qN_d}}. \tag{2}$$

If the n side is more heavily doped instead, the equation remains the same except the donor concentration needs to be replaced with acceptor concentration (and x_n is replaced with x_p).

Usually pn-junction is formed by adding a very high density of dopant atoms near the surface of the substrate. According to equation 2, the width of the depletion region is then mostly determined by doping concentration of the substrate. With high resistive (lightly doped) silicon wafers, widths of tens of micrometers can be achieved. However, the absorption depth of long wavelength photons can be much greater which increases the probability that the generated charge carriers recombine before reaching the depletion layer. For this reason, wider depletion region is often desired. The most common way to increase the depletion width is to introduce bias voltage. Applying a negative voltage to the anode, bends the valence and conduction bands so that the energy barrier between them increases [14]. As a result the depletion width increases. The larger the reverse bias the wider the depletion region. With large enough reverse bias it is even possible to extend the depletion region through the entire substrate. With too large reverse bias, the electric field in the depletion region becomes so high that either the energy barrier between bands becomes so narrow that carriers can tunnel through it or the carriers gain enough kinetic energy to ionize other atoms. The threshold for this phenomenon is called breakdown voltage and applying bias larger than that causes an exponential increase in the current flowing through the pn-junction.

Applying forward bias will have an opposite effect. Even a relatively small forward bias will quickly decrease the width of the depletion region which decreases the charge

collection efficiency. With large enough forward bias, the entire depletion region vanishes and current can freely flow through the diode. Without depletion region, almost all of the photogenerated carriers will be lost. Additionally, the forward current is much larger than the photogenerated current which means that measuring the photocurrent becomes difficult. Thus, forward bias is not usually wanted in photodiodes.

Plotting the output current of a photodiode as a function of bias voltage under different illumination intensities results into curves shown in figure 2. Equation explaining these current-voltage (IV) characteristics is [14]

$$I = I_{dark}\left(e^{\frac{qV_b}{k_BT}} - 1\right) - I_p \tag{3}$$

where I_{dark} is the dark current, V_b is the applied bias voltage, k_B is the Boltzmann constant, T is the temperature, and I_p is the photogenerated current. It can be seen that the curve will shift downwards in the presence of photocurrent. The magnitude of the shift is linearly proportional to the magnitude of the photocurrent. With forward bias the current starts to increase exponentially and influence of the photocurrent becomes negligible. However, the above equation is valid only until breakdown voltage. After that other equations need to be used to describe the exponential current increase.

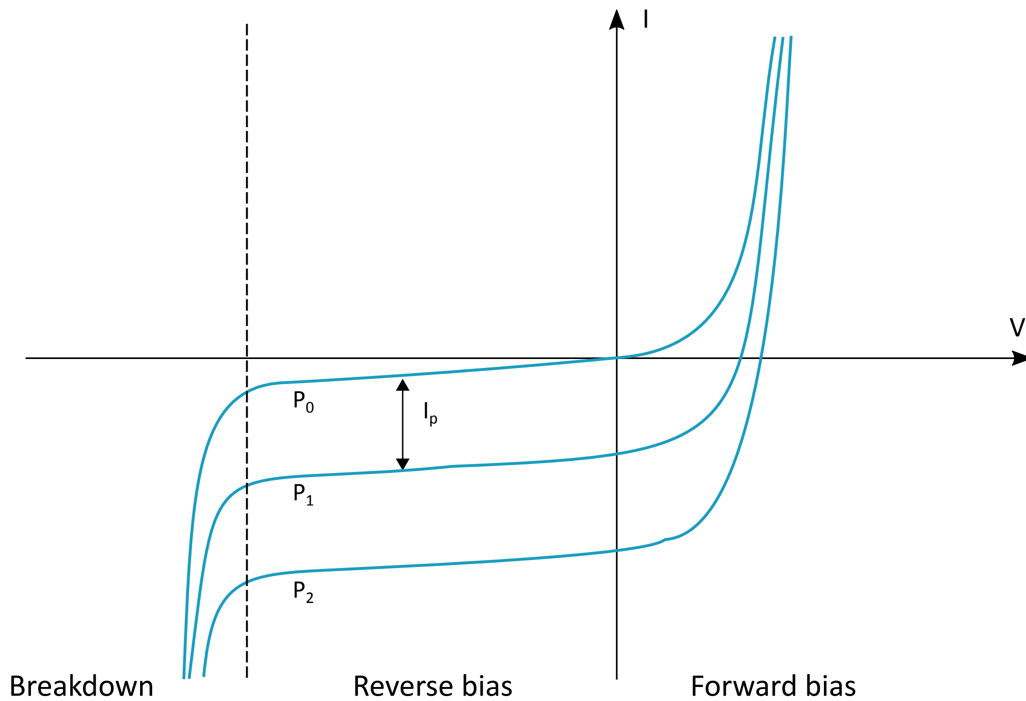

Figure 2: IV curves of a photodiode illuminated with different light intensities (P_i).

Diodes can be considered as capacitors. The p and n regions can be thought as capacitor plates and the depletion region acts as an insulator between the plates. Thus, by measuring the capacitance of a diode, it is possible to obtain information

about the depletion and doped regions. For example width of the depletion region or doping concentrations can be determined from the results. The width of the depletion region in diodes is voltage dependent which means that the capacitance is also a function of the bias voltage. Combining equation 2 and the classical parallel plate capacitor equation, results into equation for capacitance-voltage (CV) curve:

$$C = \sqrt{\frac{\epsilon_s A^2 q N_d}{2(\phi_{bi} + V_b)}} \tag{4}$$

where A is the surface area of the pn-junction. Often this equation is written as

$$\frac{1}{C^2} = \frac{2(\phi_{bi} + V_b)}{\epsilon_s A^2 q N_d} \tag{5}$$

which suggests that plotting $\frac{1}{C^2}$ as a function of bias voltage should result into a linear curve. Then the slope of the curve is

$$\text{slope} = \frac{2}{q N_d \epsilon_s A^2} \tag{6}$$

which can be used to solve the substrate doping concentration. Additionally, the built-in potential can be determined from the point where the curve intersects with the V_b axis. [14]

Common approximation is to assume that without illumination, no generation or recombination of electrons or holes occur in the depletion layer. In reality, thermal generation produces a small current called leakage current. Often it is also referred to as dark current because it is present even without illumination. However, without bias voltage and illumination, no current is seen at the output because diffusion current cancels the leakage current. If bias is applied, the currents are no longer in balance and as a result leakage current is seen at the output. Magnitude of the leakage current depends on the applied bias. This means that larger bias voltage results into larger leakage current. [14]

In reality, only a small part of the leakage current is generated in the bulk. The edges of the device chip have a large number of defects causing recombination. As a result, a relatively large leakage current is generated which is usually much larger than what is generated in the bulk. The easiest way to reduce the leakage current at the output, is to implement a guard ring structure. The idea is to fabricate an additional contact around the anode of the device. Then most of the leakage current originating from the chip edges, gets collected by the guard ring instead of the anode. Since portion of the current can bypass the guard ring and some is generated elsewhere, complete removal of leakage current is not possible when bias voltage is used.

Photodiodes can be operated in two different operation modes [16]. Figure 3 shows the circuitry required for these modes. It can be seen that the photodiode is usually connected to an operation amplifier which is used to amplify the weak photocurrent signal. In addition, there are some resistors and capacitors for filtering and controlling the current. In photoconductive mode reverse bias is applied to

widen the depletion region. In addition to increasing the collection efficiency, wider depletion region results into smaller junction capacitance. Response time is inversely proportional to the junction capacitance. Smaller junction capacitance translates into faster response time which is useful if the measured light signal changes rapidly. Unfortunately, reverse bias also introduces leakage current. If the photogenerated current is small, the leakage current can dominate and cause significant error into the measurement. Thus, photoconductive mode is not suitable for accurate measurement of low light intensities.

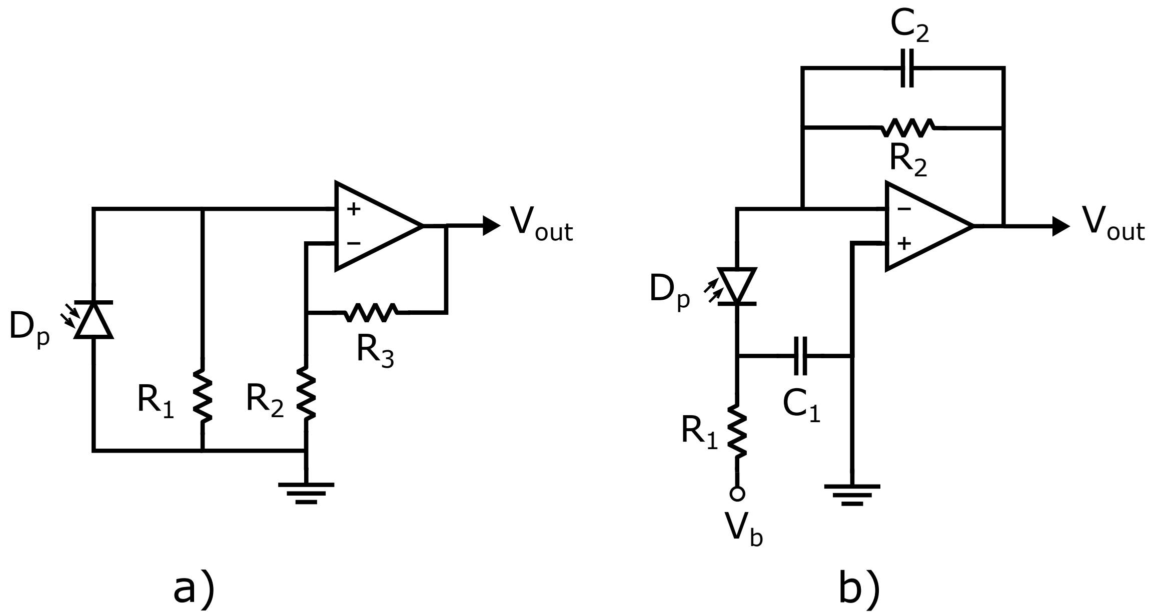

Figure 3: Circuitry needed to operate a photodiode in a) photovoltaic and b) photoconductive modes.

Another operation mode is photovoltaic mode which utilizes no bias. However, due to unideal properties of the operational amplifier in the circuitry, a small bias in the range of millivolts can occur. Therefore, some leakage current will be present but it is much smaller than in photoconductive mode. Smaller leakage current means that lower light intensities can be detected. Drawback is that the junction capacitance is larger resulting into a slower response time.

Contrary to solar cells, there is no single parameter that could be used to compare different photodiodes in the same way as efficiency can be used to compare solar cells. Instead, several different parameters are usually used. Probably the most often used property is spectral responsivity (often called also photosensitivity) which describes the response of the photodiode as a function of wavelength. Response is defined as the output current divided by the incident light power and its unit is [A/W]. Larger value is better because that indicates higher light-to-current conversion efficiency. Another way to compare photodiodes is to use external or internal quantum efficiency (EQE and IQE). EQE is defined as the ratio of collected charge carriers to the incident photons. IQE is the ratio of collected charge carriers to the absorbed photons. Thus,

IQE can be obtained from EQE by dividing it with the absorptance. EQE and IQE of an ideal photodiode is 100 % which means that all of the incident photons get absorbed and collected.

As was already discussed, leakage current is an important parameter used to characterize photodiodes. If not properly suppressed it can dominate the output current and hide the photocurrent. When calculating quantum efficiency or response, the dark current is subtracted from the collected current before making the division and thus the leakage current cannot be deduced from those values. However, in practical applications the range and accuracy of the current measurement might be insufficient for separating high leakage current and photocurrent. Additionally, the leakage current contains noise which makes the separation even more difficult. This leads into inaccuracy in the photocurrent measurement. Consequently, leakage current of the device should always be minimized.

Another important parameter in many applications is the linearity of the response. It is defined as the linearity of the output current with respect to the intensity of the incident light. With low light intensities the linearity is limited by leakage current and electrical noise while with high light intensities saturation of the photodiode is a limiting factor. The range of light intensities where the device exhibits linear behavior is called dynamic range. Sometimes it might be possible to mathematically compensate non-linearities but it requires a more complex measurement system. In order to enable as wide range of applications as possible, the dynamic range should be maximized. [17]

Photodiode should be able to perform identically in different environments and after a long time of usage. These properties are usually referred to with the term stability. It describes how identically the photodiode can operate in different temperatures and after a long time exposed to different conditions. It is normal that after some time the device performance starts to degrade and stability is used to describe how much. All the physics responsible of the photodiode operation are temperature dependent (e.g. equation 3) which means that the output current will change at different temperatures. Only way to correct the reading is to include an external circuitry that measures the temperature and performs the required adjustments. [17]

2.2 Photogeneration and recombination

Photogeneration is a process where a photon penetrates into a material and via absorption creates a free electron-hole pair (EHP). If the energy of the photon is large enough, an electron on the valence band can absorb it and transition into the conduction band. Consequently, one free EHP is created. In order to perform this transition, the energy of the photon needs to match the bandgap of the material. Any excess energy is transformed into heat or kinetic energy of the generated charge carriers.

Absorption coefficient of the material dictates how deep on average photons penetrate into the substrate before they get absorbed. The absorption coefficient is a function of wavelength [18] and the resulting absorption depths in silicon are illustrated in figure 4. It can be seen that photons with short wavelengths penetrate

only a very short distance. With wavelengths shorter than 400 nm, absorption occurs within tens of nanometers below surface. With wavelengths over 1 μm the absorption depth starts to increases quickly. Above 1.1 μm it greatly exceeds the thicknesses of typical substrates and thus silicon is considered transparent in that region. In addition, the photon energy becomes smaller than the bandgap which prevents absorption.

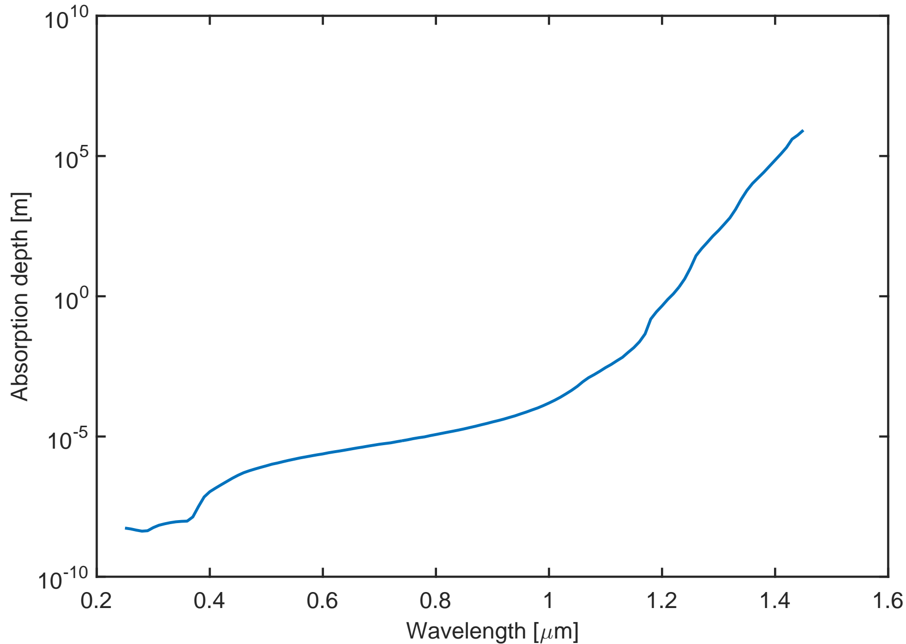

Figure 4: Photon absorption depth in silicon as a function of wavelength [18].

In order to measure the light generated current, the EHPs need to be collected from the device. Without any collection mechanism the generated free electrons will eventually fall back to the valence band and fill holes. This is called recombination. To prevent recombination, the generated holes and electrons need to be separated with an electric field. Usually a pn-junction is utilized for that purpose. The electric field in the depletion region forces the holes and electrons to the opposite sides of the junction. Practically all EHPs generated inside the depletion region will be collected. Additionally, most of the EHPs generated within one diffusion length can diffuse into the depletion region but some recombination can occur. All EHPs generated outside of that range will recombine. To ensure that most of the absorption occurs in the depletion region, depletion width needs to be optimized based on the wavelength range of the intended application. This can be achieved by optimizing the dopant profiles of the junction or by applying bias voltage. [15]

After separation, the charge carriers still need to be collected with metal contacts. Metal deposited on top of lowly doped silicon forms a Schottky contact. The contact resembles pn-junction because a potential barrier and a depletion region is formed at the interface. Thus, electrons can easily move from silicon to metal but not the other

way. Consequently, the contact is rectifying. To ensure free movement of current, the contacts need to be ohmic which are non-rectifying and have a low resistance. This can be achieved with a highly doped region under the metal. It bends the bands at the metal-semiconductor interface so much that the width of the energy barrier becomes so narrow that electrons can easily tunnel through it and move practically freely to both directions. [19]

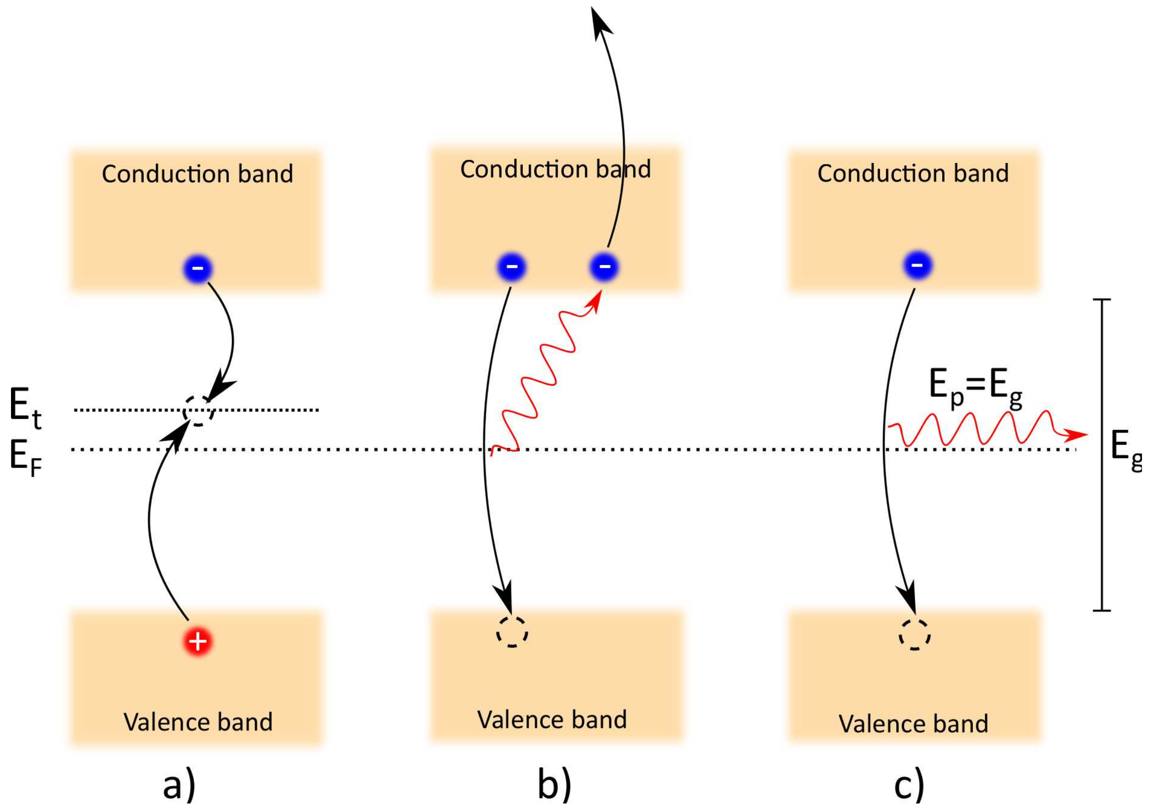

Figure 5: Illustrations of different bulk recombination mechanisms: a) Shockley-Read-Hall, b) Auger, and c) radiative recombination. E_t is the trap state energy, E_F is the Fermi energy, E_p is the photon energy, and E_g is the band gap energy.

Ideally each absorbed photon creates one EHP which means that the number of absorbed photons could be directly deduced from the collected current. In reality, some of the charge carriers are lost due to recombination. Several different recombination mechanisms exist and the three most significant processes occurring in bulk are illustrated in figure 5. In addition to bulk processes, recombination can also occur at the surface. Carrier lifetime is usually used as a metric for recombination. It is defined as the average time it takes for a charge carrier to recombine. Thus, long lifetime indicates small recombination losses. Furthermore, lifetime together with diffusivity determines the diffusion length. Long lifetime leads to long diffusion length which means that more carriers generated outside depletion region can be collected. The total lifetime when both surface and bulk phenomena are taken into

account, is defined as

$$\frac{1}{\tau_{total}} = \frac{1}{\tau_{bulk}} + \frac{1}{\tau_{surf}} \quad (7)$$

where τ_{surf} is the lifetime from surface recombination and τ_{bulk} is the total lifetime contribution of all bulk recombination mechanisms. The total bulk lifetime is defined as

$$\frac{1}{\tau_{bulk}} = \frac{1}{\tau_{SRH}} + \frac{1}{\tau_{Auger}} + \frac{1}{\tau_{rad}} \quad (8)$$

where τ_{SRH} is the lifetime from Shockley-Read-Hall (SRH) recombination, τ_{Auger} is the lifetime from Auger recombination, and τ_{rad} is the recombination from radiative recombination. In silicon photodetectors the most important mechanisms are SRH, Auger, and surface recombination. Silicon is a material with indirect bandgap where probability of radiative recombination is so small that it can be usually neglected. [20]

2.2.1 Shockley-Read-Hall recombination

Defects and impurities in the material bulk can induce energy states into the bandgap. These trap states act as recombination centers and allow charge carriers to recombine. This recombination mechanism is called Shockley-Read-Hall (SRH) recombination, named after the scientists [21, 22] who studied this phenomenon first.

Since the number of recombination centers depends on the amount of defects and impurities in the bulk, the SRH recombination rate is directly proportional to the quality of the substrate. To minimize SRH recombination, high purity substrate with a small number of defects and impurities should be chosen. During the device fabrication process all types of contamination from equipment or other sources should be avoided to ensure that the substrate quality remains good through the process.

Dopant atoms are also considered as impurities and thus SRH recombination rate is a function of substrate doping concentration [23]. Choosing a very lightly doped substrate is a good way to decreases recombination losses. In addition, making doped regions with diffusion or ion implantation creates damage to the silicon lattice. Consequently, doped regions in the active area of the device should be avoided if possible. The SRH recombination lifetime is defined as [21]

$$\tau_{SRH} = \frac{\tau_{n0}(p + n_i e^{\frac{-E_t}{k_B T_L}} + \Delta n) + \tau_{p0}(n + n_i e^{\frac{E_t}{k_B T_L}} + \Delta n)}{n + p + \Delta n} \quad (9)$$

where τ_{no} and τ_{p0} are electron and hole capture time constants, n and p are electron and hole concentrations, Δn is the injected excess carrier density, n_i is the intrinsic carrier concentration, T_L is lattice temperature, and E_t is the trap state energy level.

2.2.2 Auger recombination

Auger recombination process involves interaction of three particles. First a free electron recombines with a hole. The excess energy released in this process is then transferred to another free charge carrier. Eventually the excited carrier will return

back to its original state by thermal relaxation and thus no new charge carriers are generated in the process.

The probability of Auger recombination is proportional to the carrier density [24]. Consequently, it is significant only in highly doped regions or under high-injection conditions. However, Auger recombination is an intrinsic property which means that it is always present if the carrier density is high enough. Ultimately, if all other recombination mechanisms are eliminated, Auger recombination will become the limiting factor. Only way to decrease the losses is to avoid highly doped areas and high injection levels.

In traditional photodiodes the pn-junction is formed by diffusion which introduces a very highly doped region near the surface. In that region Auger recombination causes significant losses. Forming the junction with some other technique eliminates most of these losses and can yield better efficiencies.

The rate of Auger recombination in high-injection condition is defined as

$$\tau_{Auger,hi} = \frac{1}{(c_n + c_p)\Delta n^2} \tag{10}$$

and under low-injection level it is defined as

$$\tau_{Auger,li} = \frac{1}{c_n N_{net}^2} \qquad \text{(for n type silicon)} \tag{11}$$

$$\tau_{Auger,li} = \frac{1}{c_p N_{net}^2} \qquad \text{(for p type silicon)} \tag{12}$$

where c_n and c_p are experimentally determined Auger coefficients for electrons and holes and N_{net} is the net dopant concentration. The most commonly cited values for these coefficients [25] are $c_n = 2.8 \times 10^{-31} cm^6/s$ and $c_p = 9.9 \times 10^{-32} cm^6/s$. They are in good agreement with experimental data in highly doped silicon ($N_{net} > 5 \times 10^{18} cm^{-3}$). However, in lightly doped silicon this model predicts significantly lower lifetimes than what has been measured. With low dopant concentrations Coulomb interaction between the carriers needs to be accounted for. This can be accomplished by introducing enhancement factors g_{eeh} and g_{ehh} and multiplying the corresponding Auger coefficients with them. Based on experimental data, empirical formulas describing the enhancement factors as a function of carrier concentrations have been defined as [24]

$$g_{eeh}(n_0) = 1 + 13 \left\{ 1 - \tanh \left[\left(\frac{n}{N_{0,eeh}} \right)^{0.66} \right] \right\} \tag{13}$$

$$g_{ehh}(p_0) = 1 + 7.5 \left\{ 1 - \tanh \left[\left(\frac{p}{N_{0,ehh}} \right)^{0.63} \right] \right\} \tag{14}$$

where $N_{0,eeh} = 3.3 \times 10^{17} cm^{-3}$ and $N_{0,ehh} = 7.0 \times 10^{17} cm^{-3}$.

2.2.3 Surface recombination

On silicon surface, the monocrystalline lattice abruptly ends. Silicon atoms on the surface may not have enough neighboring atoms to achieve the optimal octet electron configuration. These missing bonds are called dangling bonds and they can easily capture nearby electrons. Thus, these dangling bonds induce trap states and can cause recombination. Essentially the recombination mechanism is the same as in SRH recombination but to emphasize that this is a surface phenomenon, it is called surface recombination. The most important difference between bulk SRH recombination and surface recombination is the defect state distribution [20]. In bulk, the trap states are discrete but on the surface they are continuously distributed across the whole bandgap. In order to use the same rate equation than with bulk SRH recombination (equation 9), it needs to be integrated over the bandgap.

Surface recombination is relevant and needs to be addressed if there are charge carriers near the surface. Especially, in solar cells and photodetectors where short wavelength photons get absorbed near the surface, surface recombination can cause significant losses. Decreasing the surface recombination rate is usually done with surface passivation which will be discussed in more detail in the next section. In addition to passivation, magnitude of surface recombination rate depends, on the area of the surface and material quality.

Instead of lifetime, surface recombination is usually quantified with surface recombination velocity (SRV). It is inversely proportional to lifetime which means that a small value indicates low recombination rate. It is not possible to directly measure SRV but it can be approximated from the measured effective lifetime with [26]

$$S_{eff} = \frac{w}{2}\left(\frac{1}{\tau_{eff}} - \frac{1}{\tau_{bulk}}\right) \tag{15}$$

where w is the thickness of the wafer, τ_{eff} is the measured lifetime, and τ_{bulk} is the bulk lifetime. Assuming infinite bulk lifetime yields the maximum value for SRV and simplifies the equation to

$$S_{eff} < \frac{w}{2\tau_{eff}}. \tag{16}$$

2.2.4 Surface passivation

Passivation of a surface means that the surface recombination rate is reduced by eliminating possible recombination sources. Two different strategies for passivation exist. The first strategy is to reduce the amount of surface trap states by eliminating dangling bonds. Usually this is achieved by depositing a thin film on top of the surface. Atoms in the thin film can form bonds with the silicon atoms on the surface and thus reduce the amount of dangling bonds. This method is commonly referred to as chemical passivation because it is based on making chemical bonds. Another strategy for passivation is to reduce the amount of free electrons or holes on the surface. If there are no counterparts available, the carriers cannot recombine. This can be achieved with an electric field which can be induced with a pn-junction near the surface or with a charged film on top of the surface. In some cases gate voltage

can also be utilized. Depending on the polarity of the electric field, it will repel most of the holes or electrons away from the surface. This method is called field-effect passivation. [27]

The most common materials used for passivation are different oxides and nitrides. Silicon oxide (SiO_2) is probably the most used material since it is easily available in standard fabrications methods. Thermally grown SiO_2 contains a positive fixed charge and thus it provides chemical and field-effect passivation simultaneously and results into very good passivation. Other popular charged materials are for example silicon nitride (SiN_x) [28] and aluminum oxide (Al_2O_3) [2].

2.2.5 Secondary ionization

In normal conditions, each absorbed photon creates one EHP which corresponds to quantum efficiency of unity. If the generated charge carrier gains large enough kinetic energy it can collide with the lattice and generate additional EHP. This way each photon can produce more than one EHP which can results into quantum efficiency above unity. The phenomenon is called impact ionization and the operation of avalanche photodiodes is based on this effect. Usually, a high reverse bias is used to induce a strong electric field which accelerates the charge carriers and initiates impact ionization. This way the output current of the photodiode can be greatly amplified. Since the occurrence of impact ionization is based on statistical probabilities, it will also introduce noise to the current. If the accuracy of the measurement is important, the amplification from impact ionization may not be beneficial after all because it can have a negative impact to the signal-to-noise ratio. [14]

Traditionally, it has been thought that the excess photon energy in photogeneration is dissipated via phonon emissions which is seen as heating. This assumption would mean that the only way the charge carriers can gain enough kinetic energy for impact ionization is to accelerate them in an electric field. However, Kolodinski et al. [29] proved theoretically that if the photons have sufficiently large energy (i.e. short wavelength), the excess energy can cause impact ionization instead of phonon emission. Assuming that all the excess energy is transferred into kinetic energy of the carrier, the absolute minimum photon energy required for impact ionization is twice the bandgap. In silicon this would include photons with wavelength shorter than ≈550 nm. However, in that case the generated carriers would not have any kinetic energy and they would recombine. Thus, in practice the photon energies need to be larger. Experiments and calculations [29–31] indicate that the threshold for impact ionization is around 3.3 - 3.5 eV which translates into wavelength between 375 - 355 nm. It would require about 30 cascaded phonon emissions to dissipate all the excess energy. Thus, impact ionization becomes the more probable relaxation mechanism and it is possible to achieve IQE exceeding unity.

2.3 Oxide charge

Oxidized silicon can contain charges that are byproducts of the oxidation process. There are several different mechanisms that affect the charges but the most important

factors are oxidation temperature, oxide thickness, and the silicon crystal orientation. The charges are usually divided into four categories: interface trapped charges, fixed oxide charges, oxide trapped charges, and mobile oxide charges. Interface trapped charges are caused by defects introduced in the oxidation process. They are located at the silicon-oxide interface and are in electrical contact with silicon. Fixed oxide charges are also located very near the interface but they are not electrically connected to silicon. Oxide trapped charge results from electrons and holes that are trapped inside the oxide. This trapping can result for example from tunneling, avalanche injection, or ionizing radiation. Mobile ionic charges result from ionized impurity atoms in the oxide. [32] The most important type of charge in our case is the fixed charge because, as the name implies it is fixed, and it will not change when voltage is applied. Thus, all discussions in this thesis related to oxide charge refer to the fixed charge if not stated otherwise.

Although the oxide charge is usually associated with thermally oxidized silicon, other oxides and nitrides can also contain the same types of charges. Thermally grown oxide contains a positive charge density that is typically below 10^{12} cm^{-2} [33]. With silicon nitride, even slightly higher positive charge densities can be achieved [28]. One material containing negative charge is aluminum oxide. When deposited with ALD even a very thin layer (tens of nanometers) can yield a very high negative charge density. With just 20 nm thick film on planar silicon surface, oxide charge density of approximately -2.5×10^{12} cm^{-2} has been achieved [3].

2.4 Induced junction photodiode

When a negatively charged oxide is deposited on top of n-type silicon, the generated electric field attracts holes towards the surface. If the field is strong enough and the doping concentration of silicon is low enough, the holes will invert a thin layer of silicon into p-type. Since the inversion layer and the bulk are in contact, they will form a pn-junction and the system will behave as a diode. The same principle also applies for p-type substrates if the oxide charge is positive.

By definition, inversion is a region where the minority carrier concentration exceeds the majority carrier concentration. This condition is often called weak inversion limit. If the minority carrier concentration also exceeds the bulk doping concentration, strong inversion is achieved. In strong inversion the width of the corresponding depletion region reaches maximum. Attempting to increase the depletion with larger oxide charge will only increase the minority carrier density in the inversion which prevents the electric field from penetrating deeper into the bulk and increasing the depletion width. Thus, when strong inversion is reached, applying bias voltage is the only way to increase depletion width. [15]

Figure 6 shows the band diagram of n-type silicon in inversion. It can be seen that the charge in the oxide on top of silicon bends the bands similarly than in a pn-junction. Band bending is described with surface potential ϕ_s which can be used to derive the thresholds for weak and strong inversion. To achieve weak inversion the Fermi level needs to be above the intrinsic Fermi-level which means that ϕ_s needs to be larger than the Fermi potential ϕ_f. For strong inversion the surface potential

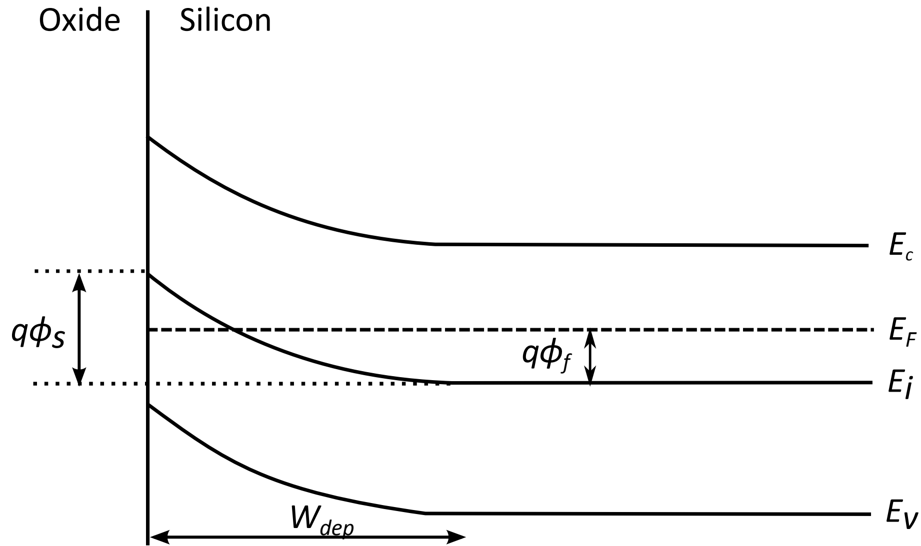

Figure 6: Band diagram resulting when negatively charged oxide is deposited on top of n-type silicon. ϕ_s is the surface potential, ϕ_f is the Fermi potential, and E_i is the intrinsic Fermi level.

needs to be twice as large as the Fermi potential which means that the threshold condition can be expressed as [15]

$$\phi_s = 2\phi_f \approx \frac{2k_B T}{q} \ln\left(\frac{N_d}{n_i}\right) \tag{17}$$

where n_i is the intrinsic carrier concentration in silicon.

Hansen [6] was the first one to apply this principle into photodiodes. Figure 7 depicts the cross section of his design. It utilizes thermally-grown SiO_2 on top of p-type silicon substrate to create an inversion layer. Metal ring is deposited on the front surface for contacting the inversion layer. Around it, a guard ring contact is deposited. To ensure ohmic contacts, n+ and p+ diffusions are made below the contacts before depositing metal. This design is very simple and the structure resembles traditional photodiodes. The only major difference is that the pn-junction is formed with inversion layer instead of doping.

The most important advantage of this type of photodiode is the elimination of doped pn-junction. When the junction is formed by diffusion or ion implantation, it causes damage to the silicon lattice. As a result, SRH and surface recombination losses will be increased. Additionally, high dopant concentration significantly increases Auger recombination rate. With induced junction these problems can be avoided and internal quantum efficiency close to 100 % can be achieved. One recent example is the predictable quantum efficient detector (PQED) [34] where induced junction photodiodes are used as a standard for radiant power measurements. It utilizes multiple induced junction photodiodes in a trap formation which collects practically all incident photons.

Resistivity of the substrate is an important parameter in induced junction photo-

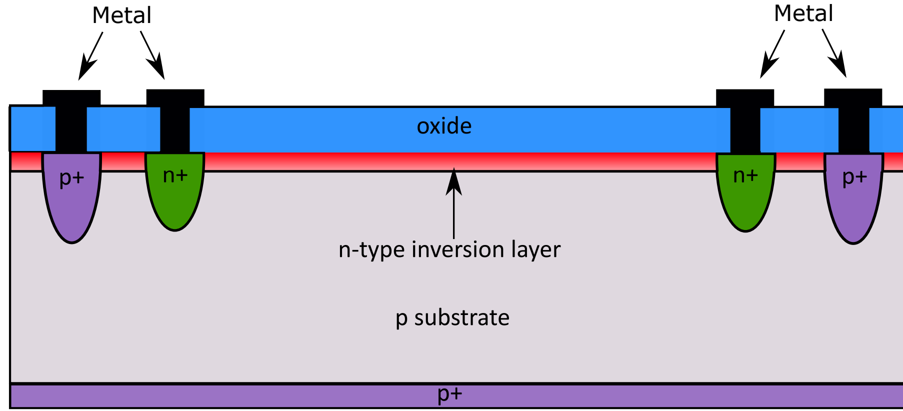

Figure 7: Cross section of the first induced junction photodiode designed by Hansen [6]. Not drawn in scale.

diodes. Lightly doped (high resistivity) wafers are preferred since strong inversion is then achieved with a lower oxide charge density and the resulting depletion layer is wider. When the oxide charge is assumed to be large enough to produce strong inversion, the width of the resulting depletion region can be approximated by combining equations 2 and 17 [15]

$$W_{max} = 2\sqrt{\frac{\epsilon_s k_B T \ln\left(\frac{N_d}{n_i}\right)}{q^2 N_d}} \tag{18}$$

where n_i is the intrinsic carrier concentration in silicon. The same equation also applies to p-type silicon when the donor concentration is replaced with acceptor concentration. In addition, high resistivity silicon has a very high quality crystalline structure and very few defects. Thus, a very long carrier lifetime is achieved which translates into an additional benefit of small recombination losses.

The thin film used for inversion formation is another important parameter in induced junction photodiodes. First of all, the material needs to be chosen so that the resulting charge has correct polarity. With n-type substrate the charge needs to be negative and positive for p-type substrate. In all previously reported induced junction photodiodes, positively charged film (e.g. SiO_2 or SiN_x) is used for inversion formation which necessitates the use of p-type substrate. However, standard in the photodiode industry is to use n-type substrate. Using p-type substrate reverses the direction of current flow. To adapt the measurement circuitry to the current direction, changes in the circuitry design are necessary. For that reason, the previous induced junction photodiodes have never gained much interest. In order to gain commercial potential, a new type of induced junction photodiode utilizing n-type substrate is needed. Thus, previously used silicon oxide and nitride needs to be replaced with a negatively charged material. One such material is ALD deposited Al_2O_3 film. Even a very thin layer of it exhibits high negative charge densities [35]. Furthermore, ALD deposition results into conformal and uniform films which also provide excellent chemical passivation. Thus, it is a very attractive material for induced junction photodiodes and it could be the next big thing in silicon photodiodes.

2.5 Black silicon

Silicon surface covered with silicon nanostructures with features comparable to the wavelength of visible light, is called black silicon (b-Si). Several different nanostructure shapes and fabrication methods exist but common for all of them is that the resulting surface appears black to naked eye. The refractive index changes gradually along the nanostructures, which almost completely eliminates reflections over the entire visible light wavelength range. Figure 8 shows the absorption measured from b-Si and planar silicon surface. Absorption is defined as

$$a = 1 - r - t \tag{19}$$

where r is reflectance and t is transmittance. Thus, high absorption means low reflectance and transmittance. From the figure it can be seen that the absorption of b-Si is very close to 100 % all the way to wavelength of 1100 nm which means that almost all reflections are eliminated. On the other hand, in planar silicon the absorption is only around 60 % indicating reflectance of nearly 40 %. The figure also suggests that the absorption in b-Si remains high with longer wavelengths than in planar silicon. This can be explained with phenomenon called optical path [36]. Due to the gradual change of the refractive index, scattering will make photons travel a longer path in silicon. Consequently, the effective optical thickness of the substrate increases and more long wavelength photons can be absorbed.

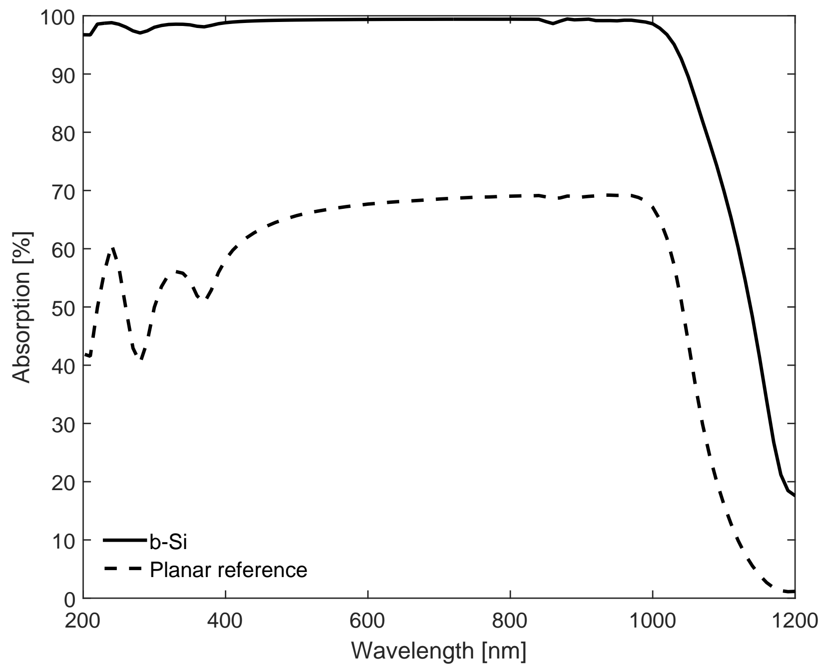

Figure 8: Absorption as a function of wavelength measured from b-Si and planar silicon samples. [2]

Currently, most of the photodiodes utilize anti-reflective coatings (ARC) to eliminate reflections but they work only for a very narrow wavelength range. Therefore, the ARC needs to be optimized based on the intended application. Since b-Si eliminates reflections on a wide range, no application specific optimization is needed. Further benefits can be obtained when the incident light comes in an angle. In traditional ARCs the only way to keep the reflectivity low with certain angle is to optimize its thickness for that angle. With other angles the reflectivity can be radically worse. In b-Si, due to the gradual change of refractive index, the reflectivity remains very small with a large range of incidence angles. Figure 9 shows measured reflectivities from b-Si with several different incidence angles. It can be seen that up to incident angles of 60° the reflectance remains under 5 %. Because of these remarkable properties, b-Si has a lot of potential in replacing the currently used ARCs in solar cells and photodetectors.

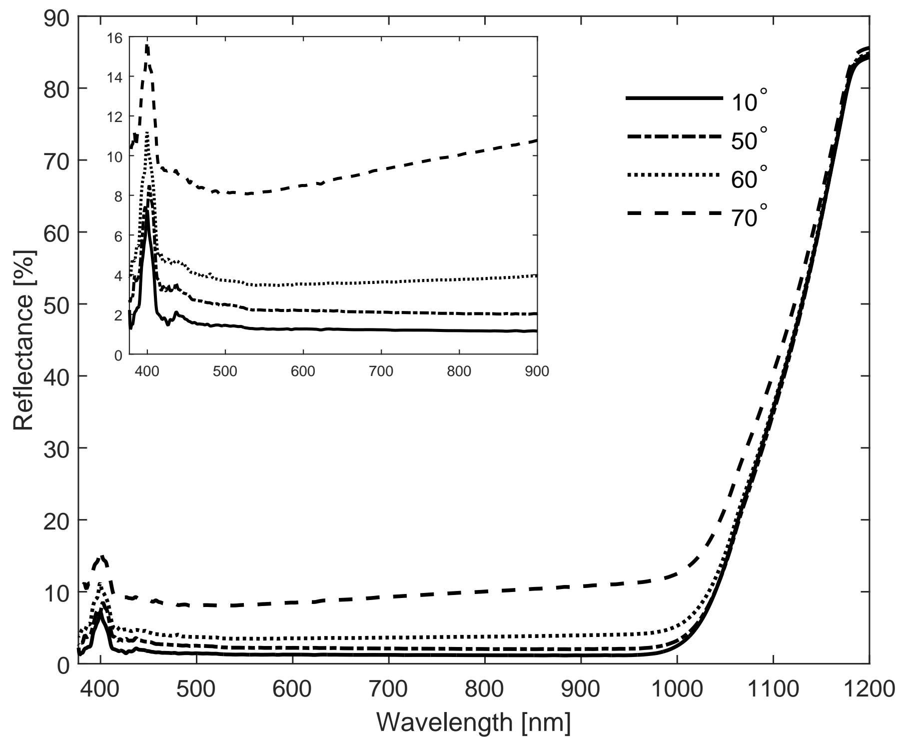

Figure 9: Reflectance of b-Si as a function of wavelength with incidence angles between 10° and 70°. The inset shows a zoomed view of wavelengths from 377 nm to 900 nm. These curves are measured in our group before this work but they are not yet published anywhere else.

Several different techniques for b-Si fabrication exists. One possibility is to deposit silver nanoparticles on silicon surface as masks and then use wet etching to form sub-micron pores on the silicon. [37] Scanning electron microscope (SEM) image of the resulting structure is shown in figure 10a. Another possibility is to coat the

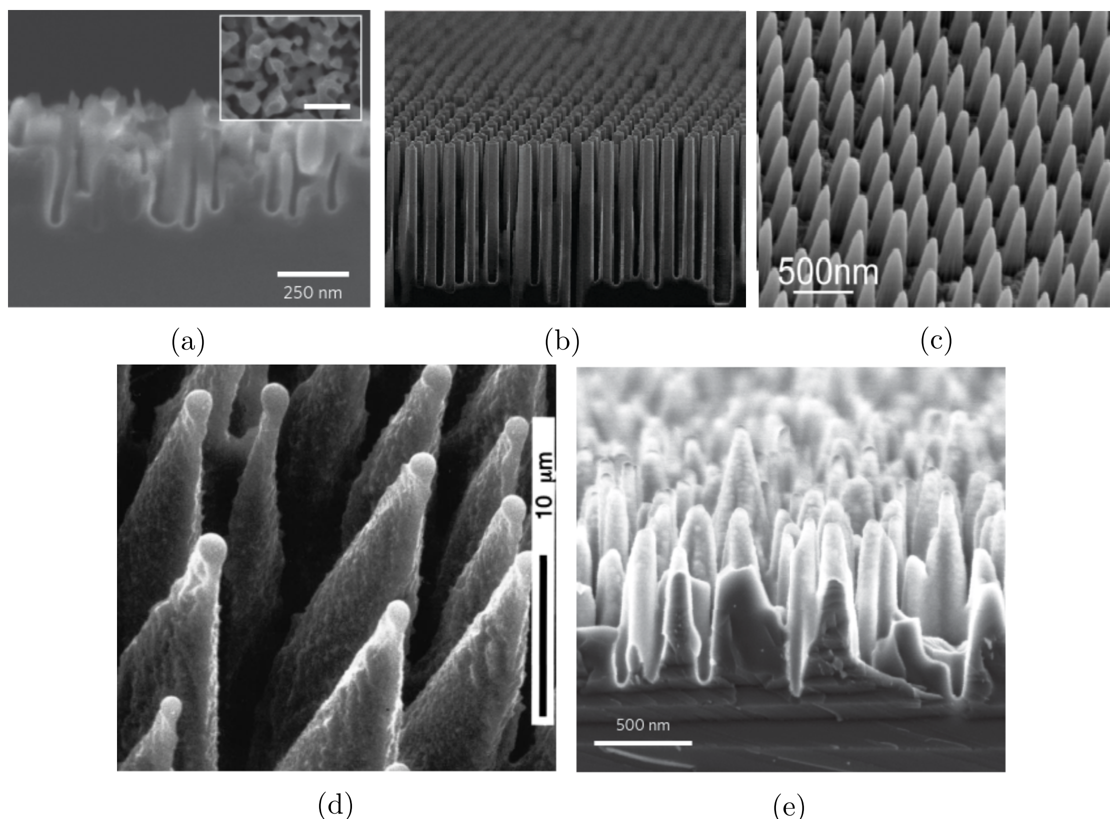

(a) (b) (c)

(d) (e)

Figure 10: Black silicon made with different techniques: a) nanopores [37], b) nanowires [38], c) nanocones [39], d) laser etched conical spikes [40], and e) random spikes [4].

surface with silica beads and use them as masks in deep reactive ion etching (DRIE) which results into systematically ordered silicon nanowires [38] shown in figure 10b. With the same principle it is also possible to make nanocones [39] (figure 10c) instead of nanowires. Common for all of the previous methods is that they use nanoparticles as an etching mask which adds at least one additional step into the fabrication process. However, it is also possible to fabricate b-Si without a separate masking step. One option is to irradiate the silicon surface with femtosecond laser pulses. [40] Figure 10d shows a SEM image of the resulting conical silicon spikes. Another maskless method is based on inductive coupled plasma - reactive ion etching (ICP-RIE) which utilizes alternating passivation and etching steps. When the passivation and etching rates are in balance the process results into trenches with vertical walls. However, with excessive passivation, parts of the passivation layer remain after consecutive etching step. The remains of the passivation layers then act as masks which leads into formation of random silicon nanospikes. [41] This is the same method used to fabricate the b-Si used in this work. Figure 10e shows a SEM image of the resulting structure.

The most important reason why black silicon is not yet used in commercial products is surface recombination. The formation of the nanostructures significantly increases the silicon surface area. Surface recombination rate is proportional to the

surface area which means that the surface recombination losses are much higher compared to planar silicon surface. For example, attempts at making solar cells covered with b-Si have resulted into efficiencies [37, 42] worse than in commercial solar cells which have much higher reflection losses.

Solution to the surface recombination problem is surface passivation. Traditionally silicon surfaces has been passivated with silicon oxides or nitrides but with b-Si the resulting passivation has not been good enough. Recent experiments with ALD deposited Al_2O_3 [3] have illustrated a much better passivation of b-Si. SRV of 7 cm/s has been achieved which is comparable to SRV of passivated planar silicon (around 4 cm/s). Good chemical surface passivation does not alone explain this excellent performance. Field-effect passivation resulting from high negative oxide charge density in Al_2O_3 is probably the reason why it yields smaller SRV than other materials. However, this does not fully explain the small difference between planar silicon and b-Si. It has been speculated that due to the geometrical effects of the b-Si spikes, the field-effect is further enhanced. Measurements seem to confirm this, since the effective oxide charge is observed to reach values approximately seven times larger in b-Si than in planar silicon. [3] With such a high effective charge the entire b-Si spikes should be completely depleted from electrons which would explain the low SRV.

3 Methods

3.1 Device fabrication

The focus of this work was mostly on the photodiode simulations and therefore the fabrication of the actual devices is only briefly discussed here. A more detailed description of the fabrication process can be found from the preceding work in [5].

The substrate is a 525 μm thick n-type double side polished silicon wafer with <100> crystal orientation. It is phosphorous doped and the manufacturer guarantees that the resistivity is >10 kΩcm. The manufacturer had measured actual resistivity of 22-29 kΩcm from the ingot before sawing the wafers. Furthermore, ≈10 ms minority carrier lifetime had been measured. Photodiodes with three different sizes were fabricated. Sizes of the active areas were 5×5 mm, 11×11 mm, and 11×22 mm. The active areas were shaped as rectangles with rounded corners.

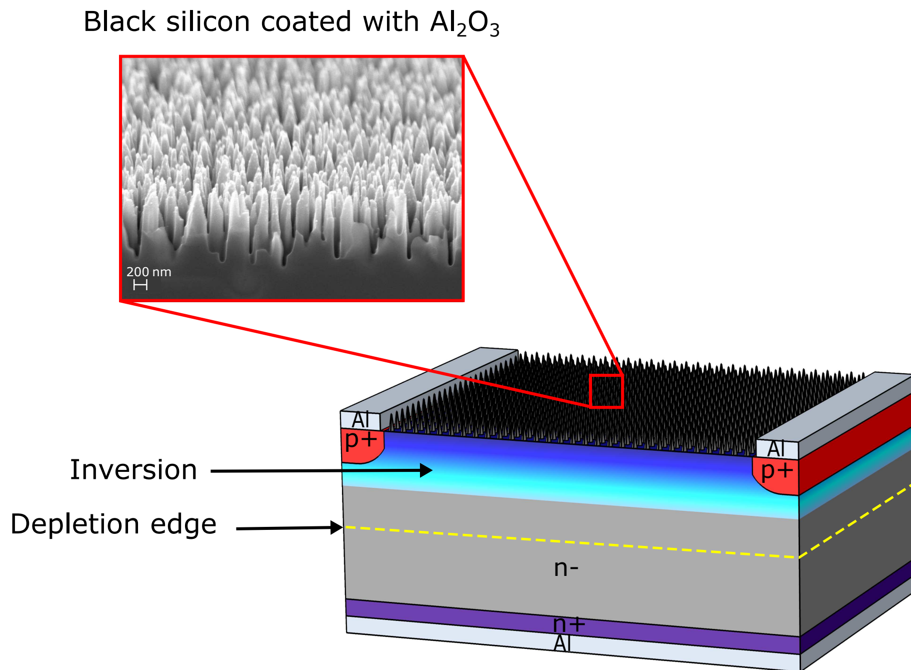

Figure 11: Cross section of the black silicon induced junction photodiode structure. Not drawn into scale.

The process starts with an oxidation and the resulting oxide is removed from the back side and patterned on the front with lithography. The front side contacts are then boron doped with ion implantation and phosphorous is implanted on the back side. The next step is to etch away the oxide mask and then grow and pattern a new one. The new mask is used to etch black silicon on the active areas of the devices with ICP-RIE. After etching away the oxide mask, a passivating Al_2O_3 layer is deposited on the front side with ALD. Next, photoresist is applied on the front

side and patterned with lithography to form openings for the contacts. Al_2O_3 is first etched and then aluminum is sputtered on both sides of the wafer to from the metal contacts. The last step is to remove all excess aluminum from the front side with lift-off. Cross section of the resulting device is shown in figure 11.

The resulting device is an induced junction photodiode which differs from other induced junction photodiodes in a couple of fundamental ways. First of all, the substrate is n-type silicon whereas all previously reported induced junction photodiodes have been based on p-type substrates. Another significant difference is that black silicon is used instead of anti-reflective coating to reduce light reflections. The surface recombination problem of b-Si is solved in this device with a thin layer of aluminum oxide. However, the Al_2O_3 layer has also another purpose. Its high negative charge is used to form the induced pn-junction. Excellent surface passivation and elimination of doped pn-junction combined with low reflectance from b-Si, result into very impressive EQE and response. Figure 12a shows the response from the fabricated photodiode measured at VTT Centre for Metrology (MIKES) and compares it with the best commercially available photodiodes. Figure 12b shows the corresponding EQE curves calculated from the responses. From the figure it can be seen that the response of our b-Si photodiode differs only a couple of percent from the ideal 100 % quantum efficiency line across the entire wavelength range. With short wavelengths the response even exceeds the 100 % line which can be explained by secondary ionization [29].

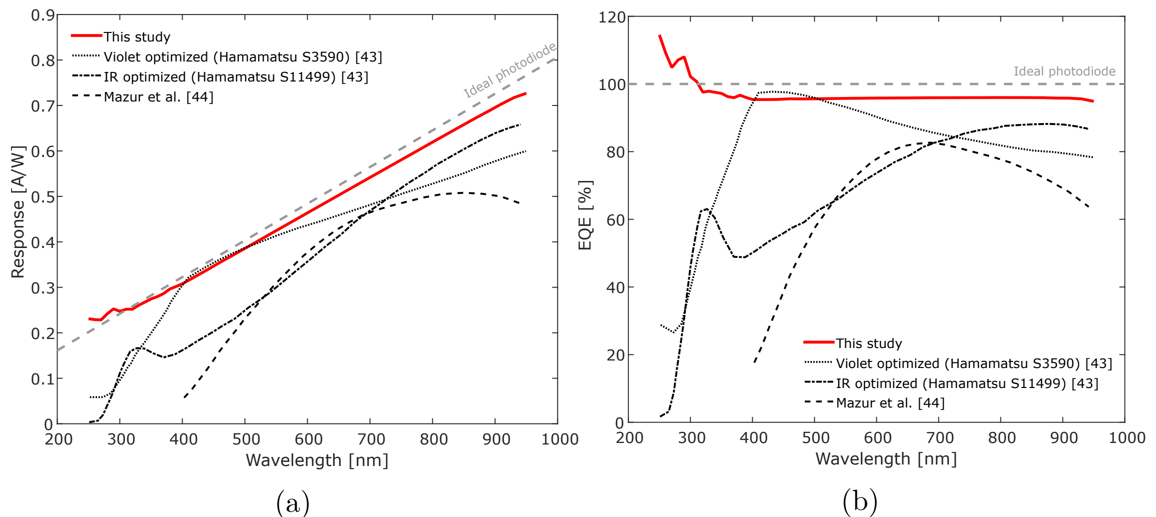

(a) (b)

Figure 12: a) Response and b) EQE curves measured from the first version of the black silicon photodetector (red line). Ideal photodiode with 100 % IQE (dashed gray line) is shown for comparison along with two commercial photodiodes (Hamamatsu S3590 and S11499) [43] and one black silicon based photodiode (Mazur et al.) [44]

For comparison, two best commercial photodiodes [43] optimized for specific applications were chosen. The Hamamatsu S3590 is optimized for violet light. From the figures it is evident that it outperforms our device around 450 nm but is inferior with all other wavelengths. The other selected commercial device was Hamamatsu

S11499 which is intended for IR applications. However, our photodiode exhibits better performance even in the IR region. The best b-Si photodiode reported so far [44], was also included in the comparison. It utilizes laser processing for etching the b-Si and for doping the pn-junction. Surface damage from the process together with insufficient surface passivation introduces recombination losses. That is why the performance of our device is superior across the entire visible light range.

3.2 Simulations

Extensive simulations were performed in order to obtain a better understanding on how the induced junction black silicon photodiode works. When trying to improve the design it is essential to understand which parameters and phenomena are important and how they affect the device operation. Simulations are also an easy way to quickly test different parameters and ideas. Although the simulations may not exactly describe the performance of the actual device, they usually provide some insight on the impact of different changes. The chosen simulator for this task was Silvaco Atlas which is a finite element simulator intended especially for semiconductor device simulations.

Generally, it is not possible to directly solve the equations describing the physics of a device with arbitrarily shaped geometry. The idea of the finite element method is to split the geometry into several small elements. Solving the equations inside these elements is easier and by combining them, solution for a complex geometry can be obtained. Entity consisting of these elements is called a mesh. Accuracy of the calculations is dictated by the quality of the mesh. It is important to have very small elements in regions which have a large impact to the device operation (e.g. regions with large electric fields or doping concentrations) to get accurate solutions. On the other hand, the number of elements is directly proportional to the required computation time. Thus, the mesh density should be optimized to be high enough in important regions but as low as possible in other regions to get an accurate solutions with a reasonable computing time. In Atlas the maximum number of elements in a two-dimensional (2D) mesh is limited to 100 000 and any mesh exceeding that will cause an error.

The first goal of the simulations was to study black silicon. Especially, the electric field induced by the charged oxide was studied. Hypothesis was that the electric field is stronger in tips of the b-Si spikes and it becomes flat quickly in the bulk. Based on that assumption, it was speculated that the spikes should be completely depleted from electrons. These were the phenomena the simulator was used to investigate in b-Si.

To ensure dense enough mesh and to keep the amount of elements within the maximum limit of Atlas, only a small block of b-Si could be simulated. Figure 13 shows the structure built for the simulations. It consists of only a few b-Si spikes that are approximated with evenly placed 2D triangles coated with a uniform 20 nm thick Al_2O_3 layer. In actual b-Si, the spike shape is not exactly triangle and the positions are random but this should give a reasonable approximation. The width of the triangles was set to 200 nm and height to 700 nm which are the dimensions observed

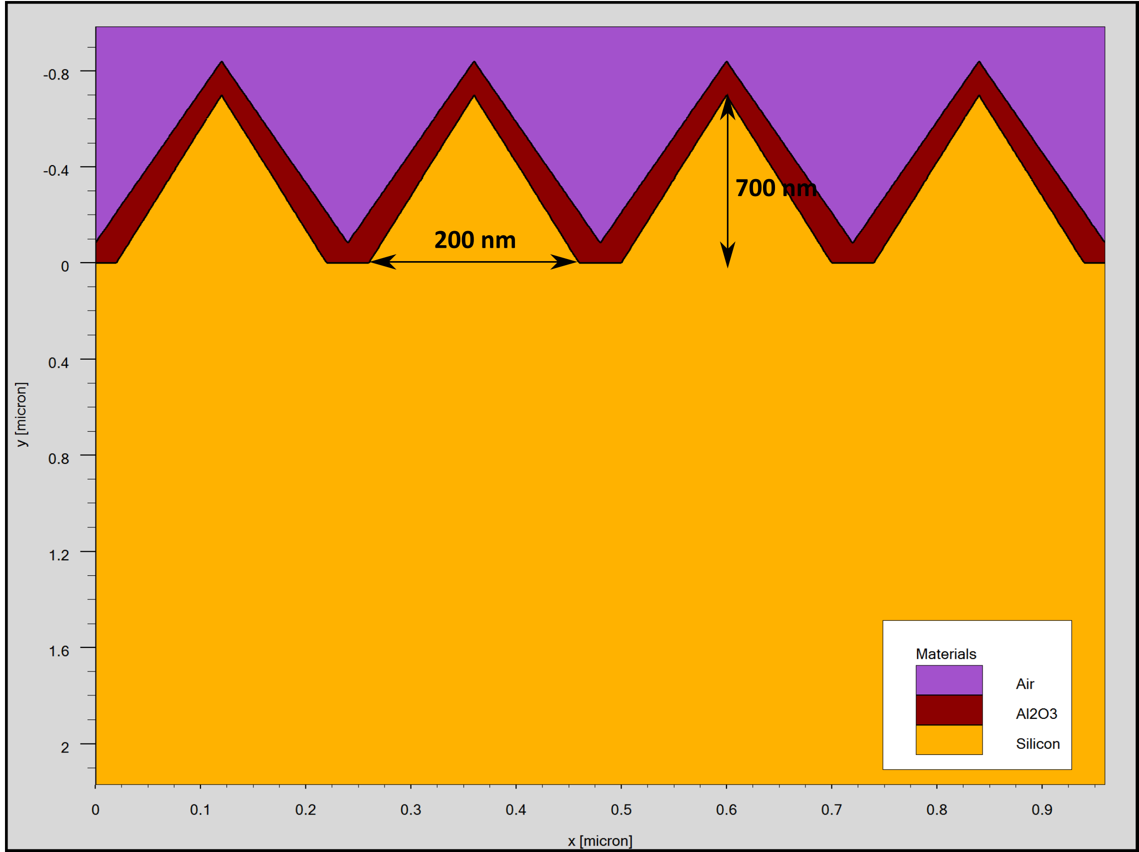

Figure 13: 2D structure used to simulate black silicon. Only the first 2 μm of the bulk is shown. In reality, the bulk is 20 μm thick.

in b-Si samples. The oxide charge of Al_2O_3 was modeled by adding a fixed charge of -2.5×10^{12} cm^{-2} into the silicon-Al_2O_3 interface. This value is experimentally determined from a planar silicon sample covered with 20 nm Al_2O_3 [3]. Triangles were placed on top of 20 μm thick silicon block which should be thick enough to represent bulk. Since the electric field is presumed to be large in the spikes, the mesh density was set denser there and coarser in the bulk.

Another model was built to simulate the operation of the photodiode. Since the active area of the device is 5 mm, it is not possible to occupy it with the approximate b-Si triangles with sufficient mesh density. Thus, only a planar photodiode could be simulated. If the assumption that the electric field is flat under b-Si is true, the planar structure should approximate it to some degree. The effective oxide charge in b-Si coated with Al_2O_3 has been determined experimentally to be approximately seven times larger than in corresponding planar sample [3]. Based on that experiment, this increased oxide charge was used in the simulations. Figure 14 depicts the structure used in the simulations. Based on resistivity measurement data received from the wafer manufacturer, the substrate donor concentration was approximated to be 2.5×10^{11} cm^{-3}. Gaussian profile with a peak value of 10^{20} cm^{-3} at 0.2 μm below the surface was used as acceptor profile under the anode metallization. The

donor profile under cathode was otherwise the same except the peak was located 0.25 μm below the metallization. The characteristic parameter which determines the shape of the Gaussian profile was defined by testing different values and comparing the resulting profiles to profile simulations made with ICECREM during device fabrication. Aluminum deposited on top of the doped regions was 0.5 μm thick.

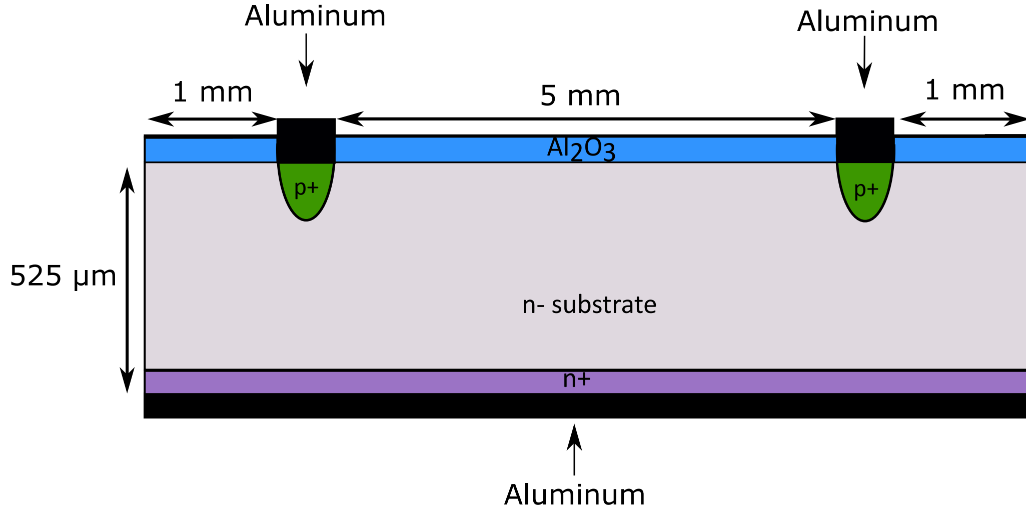

Figure 14: The first simulated planar photodiode structure. This picture is not drawn into scale in order to fit all the parts into the same figure.

The main goal of the photodiode simulations was to find ways to improve the existing device design. Especially, the leakage current should be reduced since it was relatively large in the fabricated devices. Hypothesis was that implementing a guard ring structure should effectively remove most of the leakage current and the simulations were used to prove it. Although the EQE was already almost 100 %, reflections from b-Si do not alone explain the difference of couple of percent. Finding the mechanisms causing the losses was another goal in the simulations.

By default, the solver in Atlas uses Maxwell-Boltzmann carrier statistics to solve Poisson's equation, carrier continuity equation and drift-diffusion transport model. These models are always needed but usually additional application specific models need to be added to correctly simulate different phenomena. Atlas contains a vast number of built-in models but they need to be always separately specified for the solver. Table 1 lists all of the additional models used in these simulations. Naturally, SRH and Auger recombination models need to be used because they are the main sources of losses in the photodiode. In addition to specifying SRH recombination model, SRV parameters for holes (S_P) and electrons (S_N) need to be specified for each interface where surface recombination should be considered. As was previously discussed, SRH recombination depends on the substrate doping. Atlas includes a concentration dependent SRH model but unfortunately the model is intended for relatively high doping concentrations. It did not work well in this case because the substrate is so lightly doped. However, in lightly doped silicon SRH recombination should be quite insignificant and thus a simpler SRH model with constant lifetime

Table 1: Additional models used in the simulations.

Atlas syntax	**Description**
srh	Shockley-Read-Hall recombination
auger	Auger recombination
fldmob	Parallel electric field-dependent mobility
ccsmob	Carrier-carrier scattering for low-field mobility
bgn	Bandgap narrowing
fermidirac	Fermi-Dirac carrier statistic

was used. Parallel electric field-dependent mobility accounts for carrier velocity saturation in areas with strong electric fields. It is important especially in the inversion layer. Carrier-carrier scattering for low-field mobility adds temperature, doping, and carrier-carrier scattering dependency to the mobility in regions with weak electric fields. In regions with heavy doping ($> 10^{18}$ cm^{-3}) the bandgap becomes narrower. In this case, such doping concentrations are present in the contacts and thus the bandgap narrowing model was included in the simulations. By default Boltzmann carrier statistics is used which is an approximation from Fermi-Dirac statistics. In many cases the Boltzmann is approximation is a valid option and it will make the calculations simpler. However, sometimes in highly doped regions it is necessary to use the Fermi-Dirac model and that is the reason why it was included in these simulations.

Table 2: Custom values used for some of the model parameters.

Parameter	**Value**	**Description**
τ_n & τ_p	10 ms	SRH lifetime of electrons and holes
S_N & S_P	10^5 cm/s	SRV for electrons and holes on silicon-Al_2O_3 interface
S_{CN} & S_{CP}	10^7 cm/s	SRV for electrons and holes on silicon-Al interfaces
S_{EN} & S_{EP}	10^8 cm/s	SRV for electron and holes on the device chip edges
c_n	3.919×10^{-30} cm^6/s	Auger coefficient for electrons
c_p	8.415×10^{-31} cm^6/s	Auger coefficient for holes

All the models have default values for all parameters which work in many cases but the user can also provide custom values for each parameter. All of the modified model parameter values are listed in table 2. The bulk SRH lifetime of electrons and holes was set to 10 ms based on the wafer manufacturer specification. For surface recombination simulation, Atlas uses hole and electron recombination velocity parameters S_N and S_P. Unfortunately, these parameters cannot be measured directly

and they have to be determined with other means. In a previous work related to black silicon solar cell simulations [45], these parameters have been determined with the help of simulations and those values were also used in these simulations (S_N=S_P=10^5 cm/s). Values of SRV on metal-silicon interface were also taken from the same source. Leakage current is mostly caused by surface recombination on chip edges. A large SRV value (10^8 cm/s) was used to describe that. As already discussed in section 2.2.2, the commonly used Auger recombination parameters are invalid in lightly doped silicon. Corrected values (c_n=3.919×10^{-30} cm^6/s and c_p=8.415×10^{31} cm^6/s) were calculated with equations 13 and 14.

According to Atlas manual [46], the smallest current that can be accurately modeled is approximately 10^{-16} A/μm. Any currents smaller than that will contain a significant amount of numerical noise. Although the photodiode output currents in the simulations were larger than this, the variations between simulations with different parameters were in some cases in this range. Consequently, in those cases the parameter change was assumed to have no effect.

4 Results

4.1 Black silicon simulation results

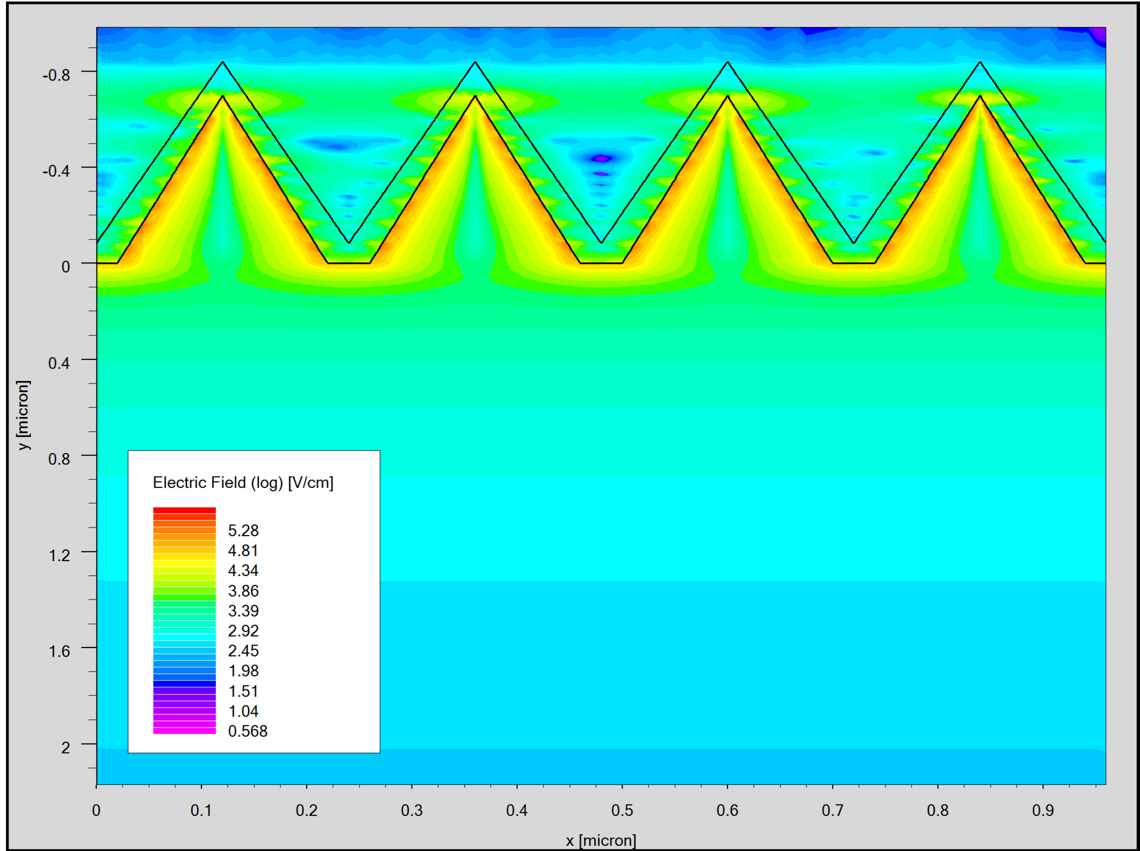

Figure 15: Simulated electric field in black silicon.

The 2D b-Si structure introduced in section 3.2 was simulated with Atlas. No illumination or any kind of bias voltage was used. The resulting electric field is shown in figure 15. It can be seen that the electric field is stronger in the b-Si spikes than in the bulk. Right under the spikes the electric field has significant variations but it seems to become flat very quickly when traversing deeper into the bulk. Figure 16 shows cross sections of the electric field from the surface and 0.5 μm below it. It is clearly visible that the electric field is flat already at 0.5 μm below the surface. Some oscillations still remain but the magnitude is insignificant and not even visible in the cross section.

Behavior of the electric field outside the device is looking strange. It is not smooth or symmetrical between different spikes. This can be explained by inspecting the mesh. In order to get a dense mesh inside the spikes, it is left quite coarse outside of the spikes. Since the electric field is relatively large outside, a denser mesh is needed there for a more accurate simulation. However, we were only interested in the electric field inside the device and thus this is not a problem.

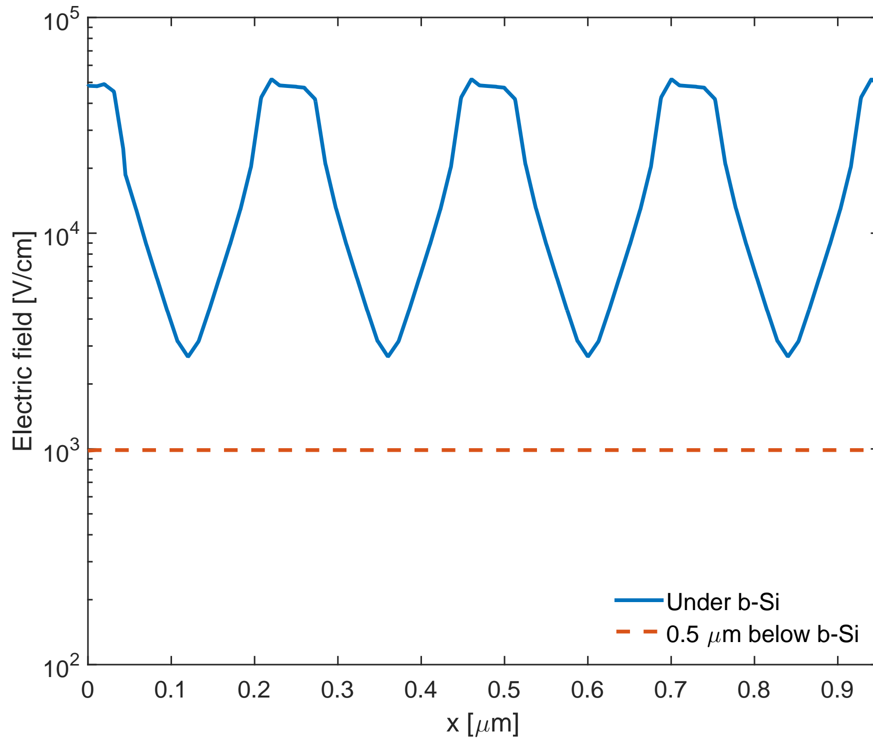

Figure 16: Cross sections of the simulated electric field right under b-Si (solid blue line) and 0.5 μm below it (dashed red line).

Electron concentration distribution resulting from the electric field is shown in figure 17. It can be seen that the electron concentration in the b-Si spikes is several orders of magnitude smaller than in the bulk. Although a small number of free electrons remain in the spikes it can be concluded that they are depleted from electrons because the number of electrons is negligible compared to the hole concentration. This result clearly supports the hypothesis about depleted spikes. Thus, the field-effect passivation should be very good in Al_2O_3 coated b-Si.

Although these results look very promising, the used model is only a rough approximation of b-Si. In reality the b-Si spike shape is not triangle. Using a more realistic shape could yield different results. The addition of third dimension to the simulation could also affect the result because then there would be a significantly larger surface area covered with charged oxide contributing to the electric field. Furthermore, the spike dimensions are so small that quantum mechanical effects should also be considered. Unfortunately, that was not possible because we did not have access to the quantum mechanics module of Atlas.

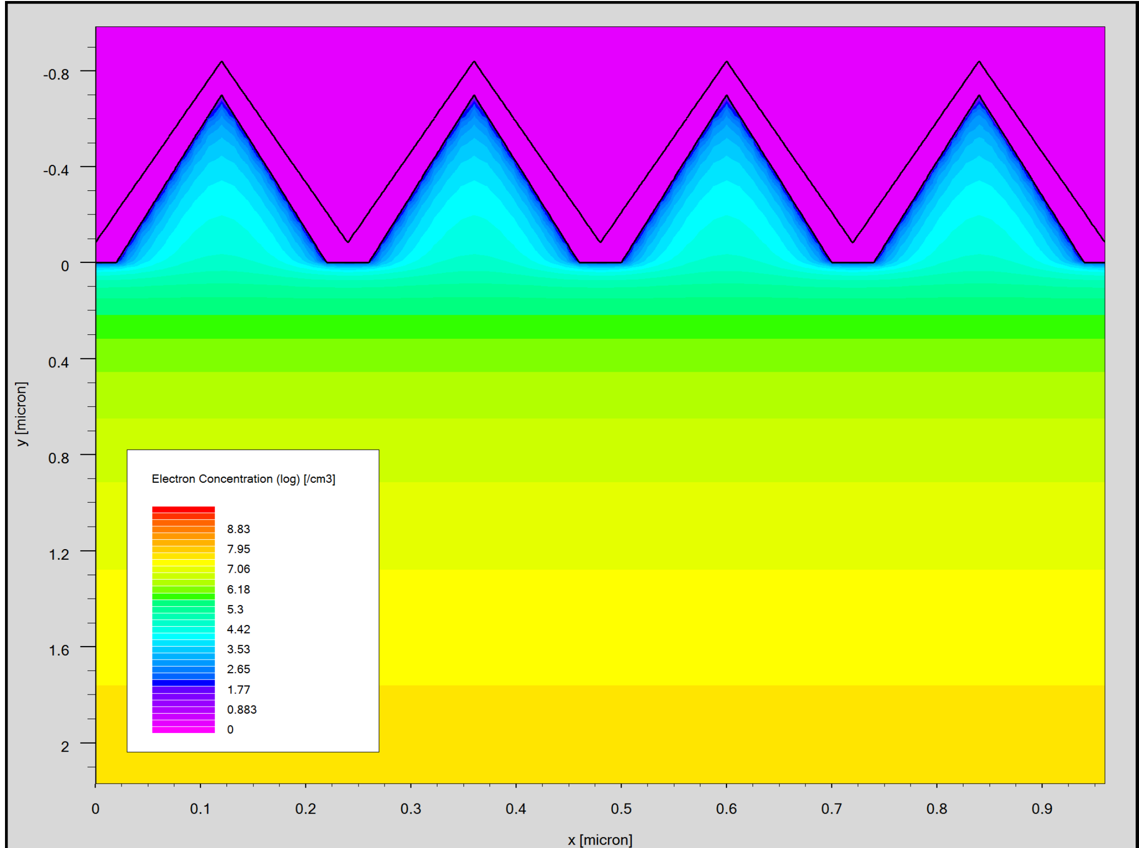

Figure 17: Concentration profile of free electrons in black silicon caused by the electric field from the charged oxide.

4.2 Planar photodetector simulation results

4.2.1 Inversion and depletion layer

The goal of the first photodiode simulations was to confirm that the charged oxide induces inversion and consequently produces a depletion layer. For that purpose, device operation was simulated with no illumination, with and without bias voltage. Figure 18 shows the simulated hole and electron concentrations along with the electric field near the device surface with no applied bias voltage. It can be seen that the electric field near the surface is very strong. As a consequence it repels almost all electrons away and attracts a considerable amount of holes. However, the magnitude of the electric field drops rapidly deeper under the surface which quickly decreases the amount of holes and increases the amount of electrons. It can be seen that the hole concentration exceeds the electron concentration until depth of about 9 μm. Since the majority carriers in the bulk are electrons this indicates inversion. Based on the inversion definitions, the depth of strong inversion is located approximately 3.5 μm below the surface and the weak inversion threshold is around 9 μm. The same simulation also indicates that the width of the depletion layer is about 30 μm with bulk doping concentration of 2.5×10^{11} cm^{-3}(not shown in the figure). This value

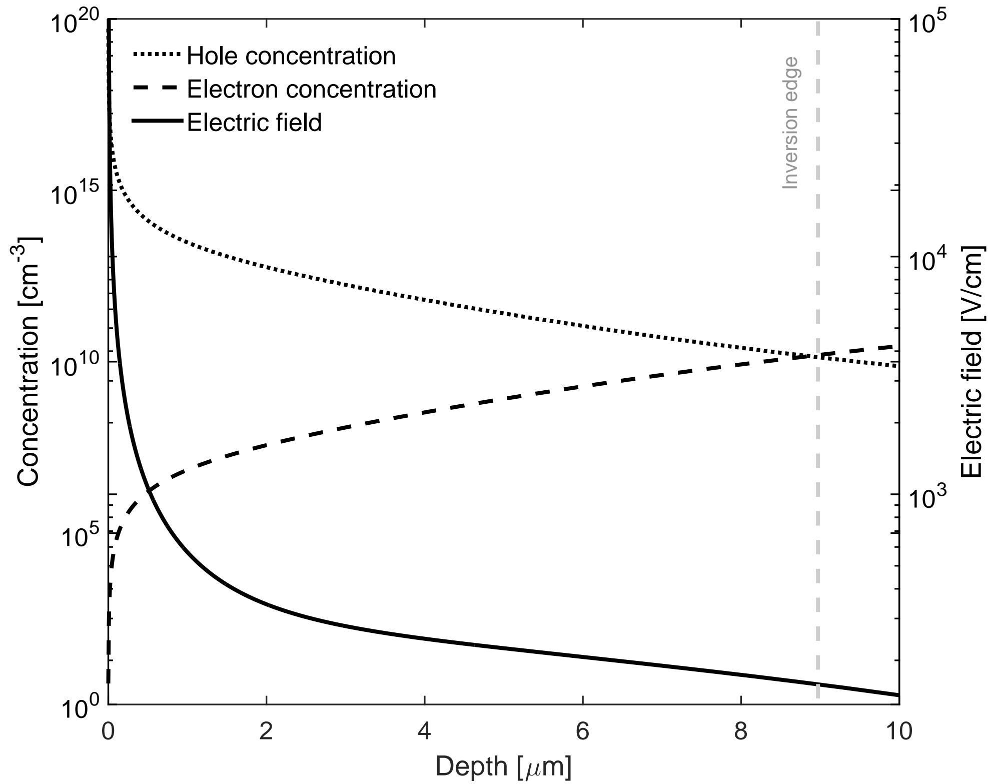

Figure 18: Simulated hole and electron concentrations and electric field near the surface of planar induced junction photodiode with n- substrate.

agrees with equation 18 which results into $W_{max} = 30.15$ μm when $N_d = 2.5 \times 10^{11}$ cm^{-3} is inserted. The simulation was repeated with different oxide charge densities. The results revealed that changing the oxide charge only affects the maximum hole concentration at the surface. The profile and depths of inversion and depletion regions remain approximately the same. Applying a low enough oxide charge density will also affect the inversion and depletion widths. The observed behavior is exactly what theory (section 2.4) predicts. After strong inversion is achieved, inversion and depletion widths reach maximum values and further increase in oxide charge will only change the hole concentration. This is illustrated in figure 19 which shows the hole and electron concentrations at the surface as a function of oxide charge density. It can be seen that when the oxide charge is larger than $\approx 4 \times 10^8$ cm^{-2}, the number of holes exceeds the number of electrons which is the weak inversion threshold. Strong inversion requires slightly larger oxide charge of $\approx 6.5 \times 10^8$ cm^{-2}. The oxide charge present in Al_2O_3 is several orders of magnitude larger than what is needed for inversion formation. This means that inversion should be guaranteed even if there are significant variations in the resulting oxide charges between processing runs. The figure also illustrates the significant increase in surface hole concentration that can be obtained if higher oxide charge density is applied.

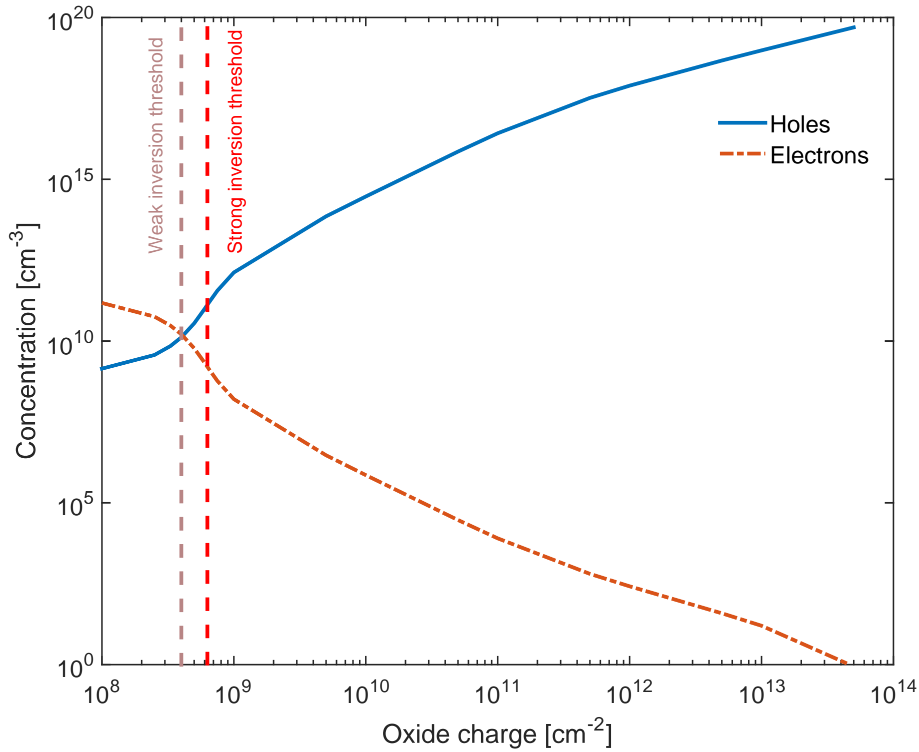

Figure 19: Hole and electron concentrations at the surface as a function of oxide charge. The dashed lines indicate threshold oxide charges for weak and strong inversion.

In traditional photodiodes, reverse bias can be used to increase the depletion width. To confirm that this behavior also applies to induced junction photodiodes, several simulations with different reverse biases were made. The results are plotted in figure 20. It can be seen that the depletion width grows rapidly if even a small bias is applied. With larger bias the growth starts to slow down and eventually it saturates as it reaches the bottom of the substrate. According to the figure, reverse bias of about 50 V is required to extend the depletion region through the entire 525 μm thick wafer. For comparison, analytical curve calculated with equation 2 is also included. The largest difference between the analytical and simulated curve is seen with large bias voltages. Since the substrate thickness is not limited in the analytical equation, no saturation is observed. Otherwise the two curves are almost identical. These results confirm that the induced junction photodiode behaves similarly than traditional photodiodes under reverse bias. Furthermore, the results confirm that equation 2 is a relatively accurate approximation of the depletion width.

CV curve of the device was also simulated to further confirm that the device is behaving as the theory suggests. Bias voltage at anode was swept from 0 V to -5 V and the resulting device capacitance was calculated. No illumination was used. The resulting CV curve is shown in figure 21. $\frac{1}{C^2}$ as a function of reverse bias is

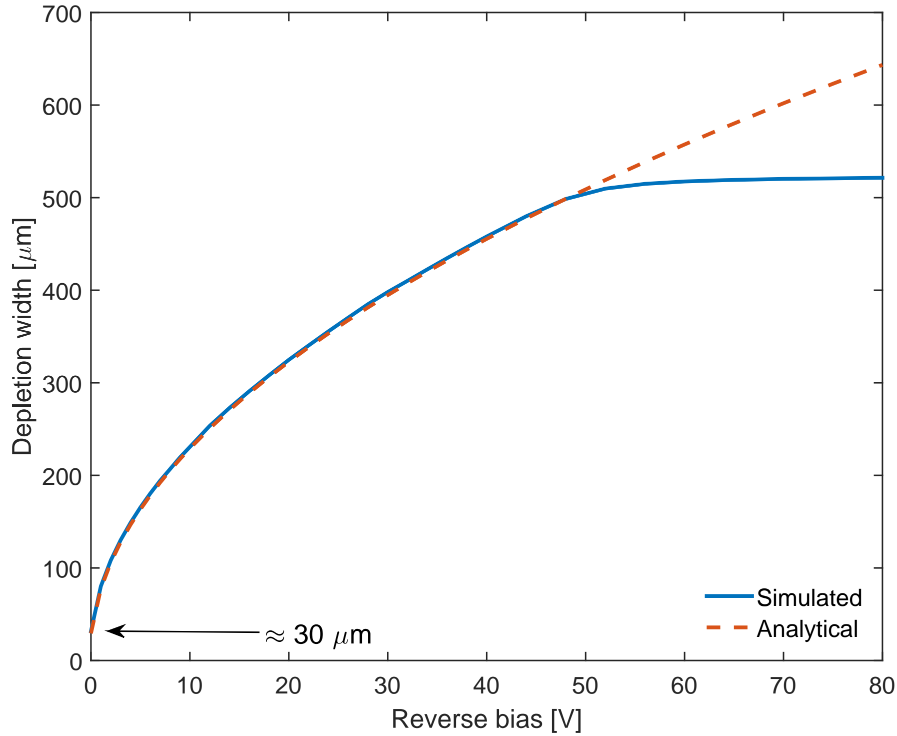

Figure 20: Simulated and analytically calculated widths of the depletion region in induced junction photodiode as a function of applied reverse bias.

also drawn. It can be seen that the capacitance decreases as reverse bias voltage is applied. As already discussed, reverse bias widens the depletion region which translates into smaller capacitance. Furthermore, the $\frac{1}{C^2}$ curve is approximately linear which agrees with equation 5. Some non-linearity is observed with bias over 2 V but in general the curve seems to agree with the theory. Next, a linear curve was fitted to the $\frac{1}{C^2}$ data to determine the slope and the voltage axis intersection point. Inserting the slope into equation 6 and solving for N_d yields 2.5×10^{11} cm^{-2} which is exactly the used substrate doping concentration. The point where the fitted curve intersects with the voltage axis yields the surface potential required for strong inversion. The resulting value was 0.1664 V which is identical to what equation 17 gives when $N_d = 2.5 \times 10^{11}$ cm^{-2} is inserted.

For further comparison, approximate curves calculated analytically from equations 4 and 5 are included in the figure. Overall difference between analytical and simulated curves is very small but with zero bias the simulated capacitance is considerably higher than the analytical. Figure 20 confirmed that the depletion width without bias is around 30 μm which according to equation 4 corresponds to capacitance of 168 pF. Thus, there must be something else affecting the capacitance when no bias is applied. Since the doped regions under contacts will also form pn-junctions, the resulting capacitance could be responsible for the observed increase in the total

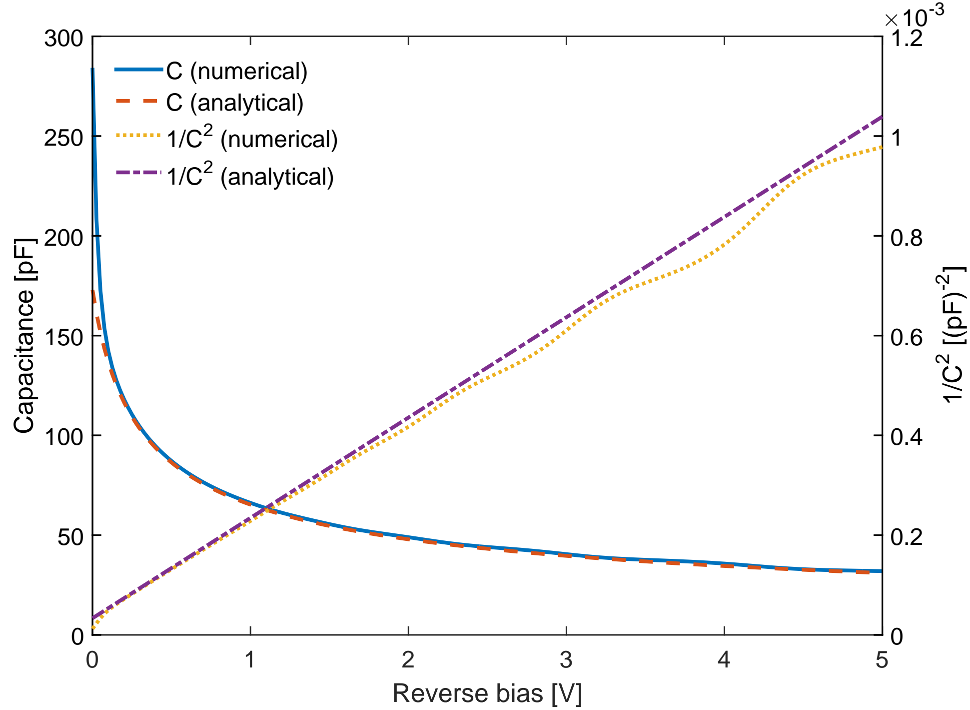

Figure 21: Simulated CV curve and the corresponding $\frac{1}{C^2}$ curve. For comparison, analytically calculated curves are also included.

capacitance. This hypothesis was tested by decreasing the doping concentrations. The results showed that with doping concentration lower than 1×10^{15} cm^{-3}, the total capacitance with zero bias decreased. With bias, no significant change was observed. This supports the speculations that contact capacitance is causing the increase in total capacitance.

4.2.2 Inversion layer sheet resistance

Instead of normal resistivity, the resistivity of a thin film is commonly described with quantity called sheet resistance which do not depend on the area of the film. In solar cells the sheet resistance of the emitter is a very important parameter which has a great influence on the efficiency. Large sheet resistance will cause severe losses which decreases efficiency. However, too small sheet resistance can promote Auger recombination and cause losses. Thus, controlling the exact emitter sheet resistance is important. Photocurrents in photodiodes are much smaller and thus the role of the sheet resistance is not very significant. However, one goal of the simulations was to determine if the sheet resistance of the inversion layer in b-Si is in a proper range for solar cell applications. For that reason, sheet resistance with several oxide charge densities was simulated. Atlas cannot directly calculate the sheet resistance but it can be easily calculated afterwards from the simulated hole concentration profile in

the inversion layer with [47]

$$\frac{1}{R_{sh}} = \int_0^{x_j} q\mu_p(N(x) - N_b)dx \tag{20}$$

where x_j is the depth of the inversion layer, μ_p is the mobility of holes, $N(x)$ is the hole concentration as a function of depth, and N_b is the bulk doping concentration.

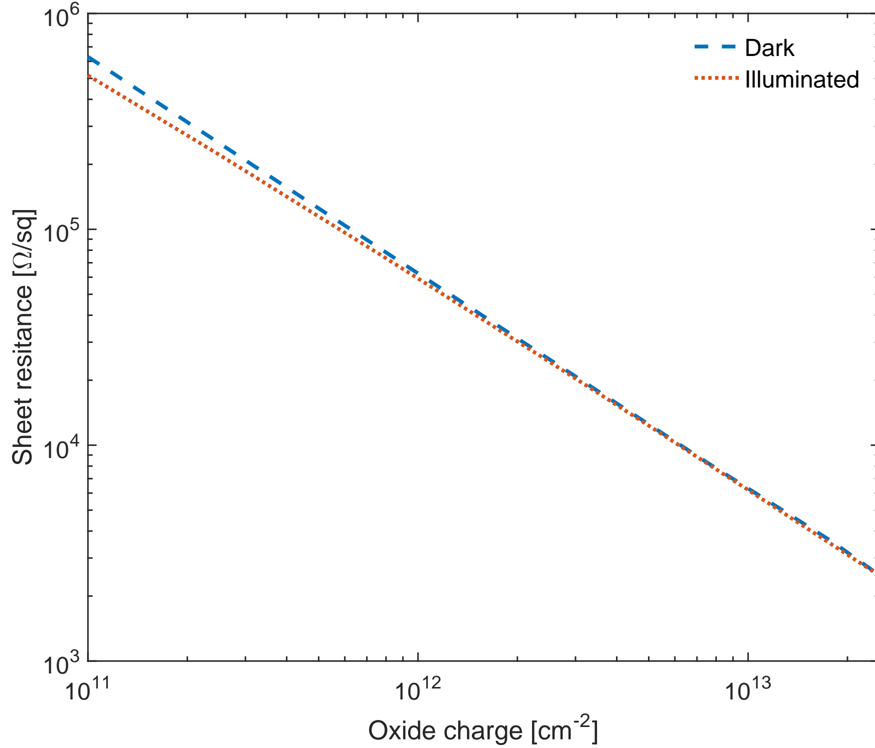

Figure 22: Simulated sheet resistance of the inversion layer in the dark and under 100 mW/cm^2 illumination as a function of oxide charge. Constant hole mobility of 100 cm^2/Vs was used in the calculation of the sheet resistance from the hole concentration profile.

The resulting sheet resistances as a function of oxide charge density in the dark and under 100 mW/cm^2 illumination are plotted in figure 22. Wavelength of the used light was 600 nm. It can be seen that increasing the oxide charge decreases sheet resistance in both cases. This can be explained by inspecting the hole concentrations near the surface. From equation 20 it is evident that larger hole concentration will yield smaller sheet resistance. As was already discussed, after the threshold of strong inversion is reached, further increase in the oxide charge will only increase the hole concentration near the surface. The widths of the depletion and inversion layers remain approximately the same in strong inversion regardless of the oxide charge density. This means that the sheet resistance should decrease with larger oxide charge, as was seen in the simulation results. Furthermore, the simulated curves

seem to be quite close to linear which means that for example doubling the oxide charge will approximately cut the sheet resistance in half.

Under illumination the sheet resistance is lower than in the dark. This can be explained with the high number of photogenerated charge carriers. The concentration of generated electrons can exceed the bulk doping concentration which will lead into decrease in inversion and depletion widths. However, the generated holes will be attracted towards the surface and they will increase the hole concentration in the vicinity of the surface. Because the hole concentration is several orders of magnitude larger near the surface than in the bulk, the first few hundred nanometers dominate the magnitude of the sheet resistance. Thus, the enhanced surface hole concentration decreases the overall sheet resistance as long as the oxide charge is large enough to induce a strong inversion. However, the difference between the two curves is not very significant. With lower oxide charge densities some difference exists but with higher values almost no difference can be detected.

Since the geometry of b-Si enhances the electric field resulting from the oxide charge, effective surface charges of over 10^{13} cm^{-2} could be achieved. Figure 22 suggests that the corresponding sheet resistance could be below 5 kΩ/sq. Werner et al. [48] performed similar simulations for an induced junction solar cell and the resulting sheet resistance values were similar to the ones obtained here. They used a planar surface covered with Al_2O_3 and a substrate with higher doping concentration of 10^{15} cm^{-3}. This means that in the high resistivity wafers used in this study the actual sheet resistances could be even lower. With their test solar cell, Werner et al. achieved efficiency of 18.1 % but according to their simulations it could be potentially improved up to 26.3 % by improving the fabrication process. As was seen, the inversion layer sheet resistance should be smaller in b-Si than in the planar surface used in [48]. Thus, a solar cell utilizing induced junction from Al_2O_3 coated b-Si, could potentially reach an even higher efficiency.

The photogenerated current travels to the contacts in the inversion layer and thus losses caused by the resistance of the inversion can lead into a potential difference across the surface. This potential difference is basically the same thing as applying a small forward bias. When operating in photovoltaic mode, forward bias especially should be avoided because, as equation 3 suggests, the current flowing through the device will increase exponentially. Even a relatively small forward bias can cause a large offset to the output current. Simulations were used to investigate how large biasing should be expected in the induced junction photodiodes. The simulations were performed by illuminating the device with different intensities and inspecting the electrical potential across the surface. Figure 23 depicts the results. A clear potential difference is observed. However, the magnitude is only 10 mV with light intensity of 10 mW/cm^2. With lower intensities the potential difference is significantly smaller. When operated in photovoltaic mode, unideal operational amplifier can cause biasing with similar magnitude. Consequently, the voltage difference from inversion layer resistance will not add significant additional bias.

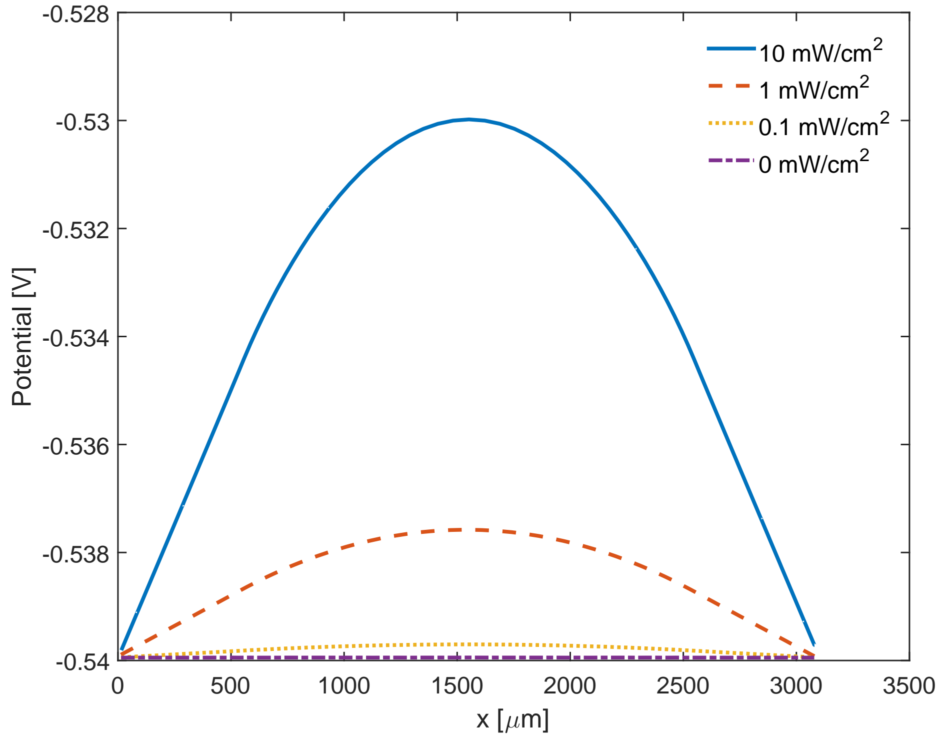

Figure 23: Cross section of the electrical potential on the photodiode surface between electrodes with different light intensities.

4.2.3 Spectral response

After confirming that the induced junction acts as a photodiode, the spectral response of the device was simulated. Several different parameters were varied to study their influence to the response. 2 mm wide light beam with power density of 1 mW/cm^2 was used to illuminate the center of the device. The current collected at the electrodes was calculated while sweeping the light wavelength across the visible light range. IQE was calculated by dividing the resulting current by the total generated photocurrent. In the intended computed tomography applications the photodiodes are operated in photovoltaic mode and thus no bias voltage was used in these simulations either. A typical IQE curve obtained with the model is shown in figure 24. For comparison, IQE curve calculated from figure 12b is included. To emphasize the advantage of induced junction, IQE curve simulated with a photodiode utilizing doped junction is also included in the figure. It can be seen that the photodiode with doped pn-junction achieves comparable performance only in the long wavelength region. With shorter wavelengths the absorption occurs near the surface where Auger and surface recombination cause severe losses and results into poor IQE. However, the difference seen here is probably overestimated because the pn-junction doping is not optimized. Instead, the same doping profile used under contacts was directly applied into the active area. The figure also shows that with wavelengths longer than 450

nm, the simulated IQE of the induced junction photodiode is slightly higher than the measured. This means that there is still some phenomenon not included in the simulation which causes losses in the actual device.

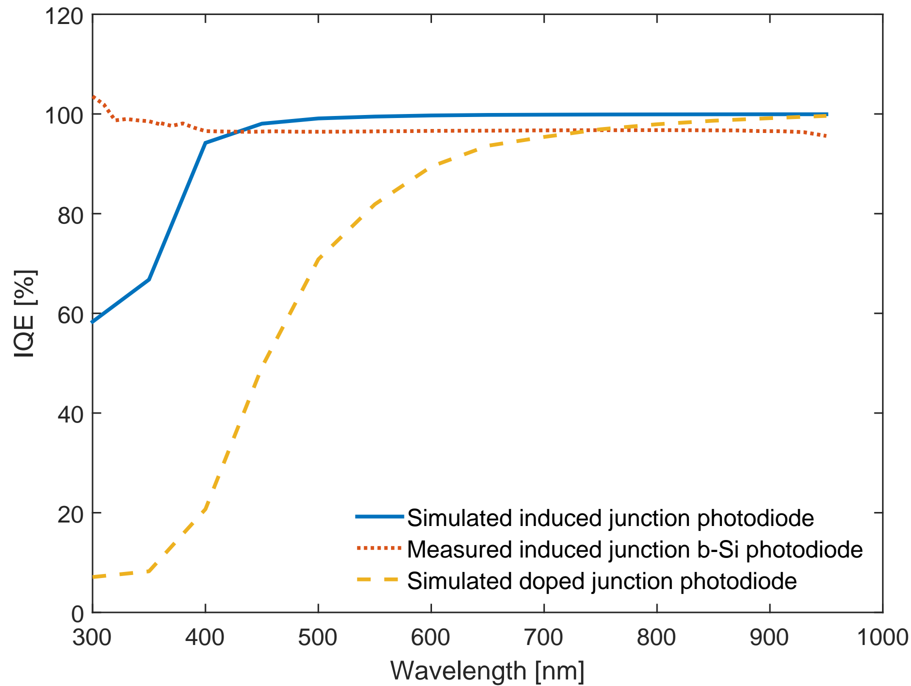

Figure 24: Simulated (solid blue line) and measured (dotted red line) IQE of the induced junction photodiode. For comparison, simulated IQE of a photodiode with pn-junction formed by doping is included (dashed yellow line). The IQE of the actual photodiode was calculated from measured response and reflectance data.

The figure shows that between wavelengths of 500 nm and 950 nm, the simulated IQE of induced junction photodiode is over 98 %. With wavelengths shorter than 400 nm, the IQE drops radically. From figure 4 it can be seen that the absorption depth is less than 100 nm in that region. A natural conclusion would be to blame surface recombination for the losses. However, applying SRV of zero to the surface does not yield so large change in the IQE. After some investigation, the probable source of the difference was found. The IQE is calculated by dividing the collected current with a parameter called available photocurrent which is given by Atlas. It is calculated analytically based on the light beam and the absorption coefficient in silicon. However, when calculating the currents flowing in the device, Atlas uses photogenerated current that is calculated in each mesh element by integrating the photogeneration equation over the element [46]. Consequently, the value of available photocurrent does not depend on the mesh but the collected current does. When the absorption occurs near the surface, there are only a few mesh elements where the photogenerated current is calculated which means that a significant error can occur if the mesh density is insufficient. With longer wavelengths the absorption

occurs in a much greater area which means that a single mesh element does not have such a high influence on the result. Thus, with long wavelengths the analytical value should be quite accurate. To test this hypothesis, a smaller version of the simulation structure was built in order to test increased mesh densities. Several simulations with different mesh element heights near the surface were made and IQEs at short wavelengths were compared. The results are shown in figure 25. They seem to support the speculations. By increasing the mesh density right below the surface, a considerable increase in IQE was observed with short wavelengths. On the other hand, with longer wavelengths (> 500 nm) practically no change occurred. It seems that the IQE could be increased to the same level with short wavelengths by decreasing the mesh element size even further. Unfortunately, it is not possible to increase the mesh density in the fully-sized photodiode model due to the mesh element limit in Atlas. Height of 20 nm was the smallest that could be used in that model. This means that the output currents obtained with the fully-sized model can contain significant errors in the short wavelength region.

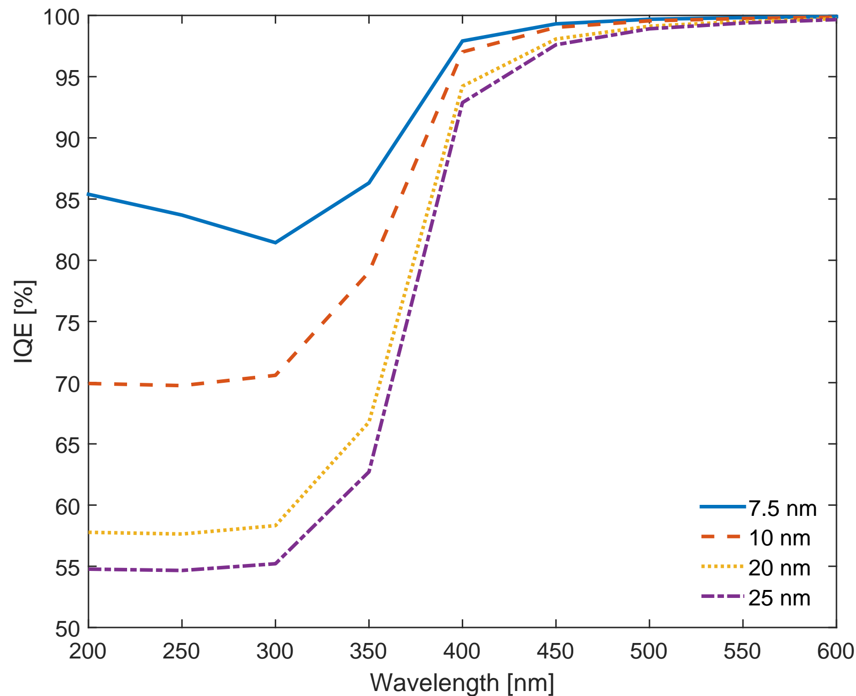

Figure 25: IQE under short wavelength illumination with different mesh element heights near the surface.

Although the insufficient mesh seems to mostly account the small simulated IQE with short wavelengths, it does not explain why the measured IQE reached values even over 100 %. Most likely this is caused by secondary ionization discussed in section 2.2.5. This phenomenon is not included in the simulations which is another reason why the simulated IQE is radically lower than the measured. Including impact

ionization model in the simulations was tested but the measured behavior in the short wavelength region could not be reproduced. Enhancing the electric field by increasing the oxide charge or applying bias voltage was the only way to obtain significant impact ionization rates. Several percent increase in the IQE was observed only when oxide charge larger than 10^{15} cm^{-2} was applied. However, the increase in IQE was observed with all wavelengths. This suggests that the excess photon energy is not the reason for impact ionization. Instead, the electric field becomes so large near the surface that it accelerates the charge carriers enough for impact ionization. Atlas includes several different models for impact ionization and all of them lead into similar results. Either the default parameters in the models are not valid in this case or the models are not suitable for simulating this phenomenon.

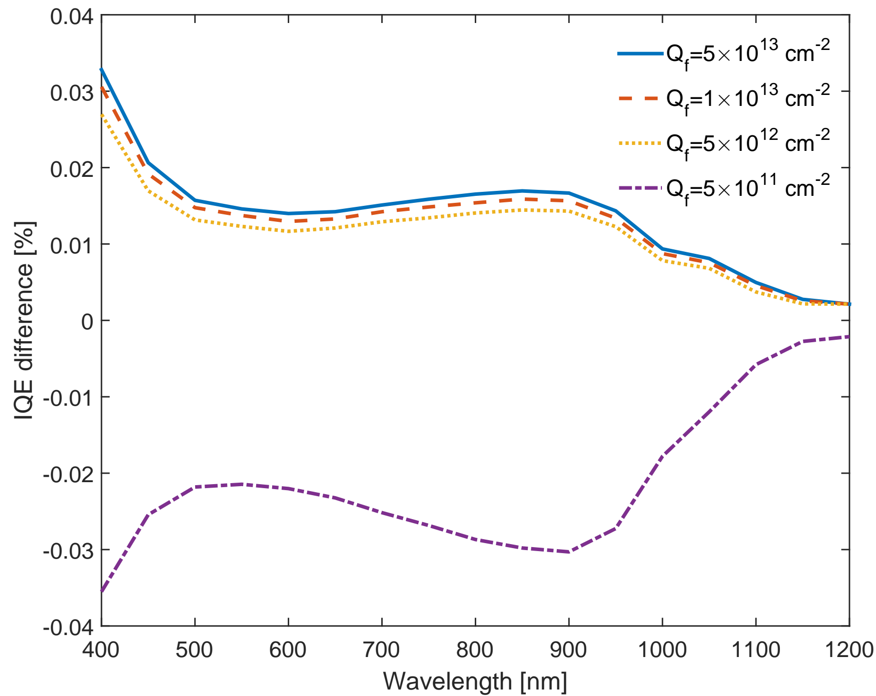

Figure 26: IQE differences as a function of wavelength obtained with different oxide charge magnitudes. Comparison is done with oxide charge of 10^{12} cm^{-2}. Negative values indicate decrease in the IQE and positive values indicate increase.

The first parameter that was varied in the spectral response simulations was the oxide charge. As was already shown, as long as the oxide charge is large enough to induce strong inversion, increasing the oxide charge will not significantly change the inversion layer or the associated depletion region. Thus, the magnitude of the oxide charge should not have a large effect on the spectral response. Figure 26 shows the simulated IQE differences with different oxide charges compared to 10^{12} cm^{-2}. It can be seen that increasing the oxide charge will increase the IQE but the magnitude of the difference is relatively small. With oxide charge larger than

-5×10^{12} cm^{-2}, almost no improvement to IQE is achieved. It can be seen that the largest IQE improvements are achieved with short and long wavelengths. The short wavelength photons get absorbed near the surface where the electric field is largest. Thus, increasing the electric field enhances field effect passivation and improves the charge separation efficiency which are seen as an improvement in IQE. The same applies for long wavelengths. Deep in the bulk the electric field is small and thus even a relatively small increase can improve the performance. However, it can be seen that with wavelengths greater than 900 nm, the IQE difference starts to decrease. In that region an increasing number of photons can penetrate the entire substrate and around 1100 nm the photocurrent approaches zero. Thus, magnitude of the oxide charge does not matter because there are almost no carriers to be collected. The conclusion from these results is that the higher oxide charge does improve IQE but the magnitude of the improvement is almost negligible.

However, another simulation with different light intensities revealed that with higher light intensities the magnitude of the oxide charge has a larger influence. As was already discussed, the concentration of photogenerated carriers can exceed the bulk doping concentration which results into decrease in inversion and depletion widths. As a result the IQE starts to drop when the light intensity exceeds 10 mW/cm^2. Larger oxide charge induces a stronger inversion and it takes more photogenerated charge carriers to negate it. Consequently, a high IQE can be maintained with higher light intensities.

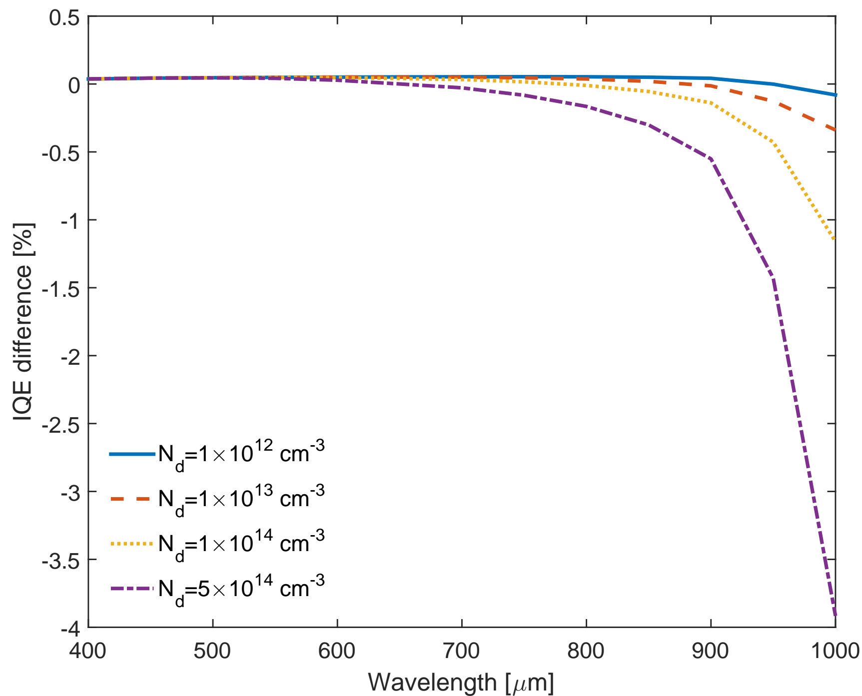

Figure 27: Differences in IQE as a function of wavelength with different substrate doping concentrations. Comparison is done with doping concentration of 10^{11} cm^{-3}.

The next tested parameter was substrate doping concentration. IQE was simulated with several substrate doping concentrations and the results are shown in figure 27. It shows the differences in IQE compared to 10^{11} cm^{-3}. It is evident that with long wavelengths lighter doping is better. Higher doping concentration results into narrower depletion region which decreases IQE on long wavelengths because a larger portion of the charge carriers are generated outside the depletion region. In addition, the bulk lifetime decreases when the impurity concentration is increased which also diminishes the IQE. This means that as high resistive (i.e. lightly doped) substrate as possible should be used if good performance in long wavelength region is needed. The only drawback is that manufacturing high resistive silicon is challenging which increases the cost of the wafers.

4.2.4 Effects of contact size and doping profile

Photodiode is useless if the photogenerated current cannot be properly collected out of the device. Thus, it is essential to design the contacts so that they do not cause any additional current losses. To ensure good collection efficiency, the contacts need to be ohmic which is achieved by heavily doping the silicon under the metal contacts. Simulations were used to investigate how contact width and doping profile affect the spectral response.

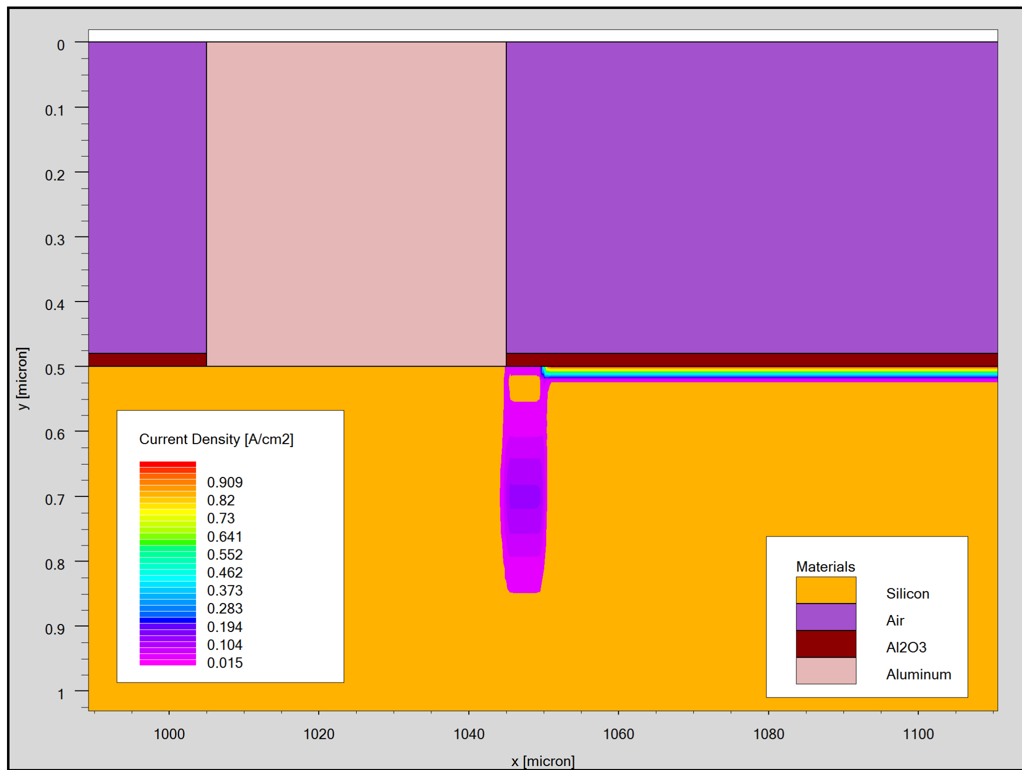

Figure 28: Photogenerated current density near front electrode. Peak of the contact doping is located 0.2 μm below metal.

Figure 28 shows simulated current density near the front contact. It can be seen that outside contact area, the current travels very near the surface. When the current approaches contact, it starts to spread on a larger area. Examination of the contact doping profile reveals that the current spreads across the doped region with maximum located at the peak doping concentration. Thus, the current seems to follow the doping profile. This was confirmed by changing the location of the dopants and inspecting the current density. Each time the maximum of current density and doping profile were at the same position. This implies that the charge carriers will travel a longer distance if the dopants are deeper below the surface which could result into higher recombination losses. The significance of the phenomenon was simulated by varying the position of the dopants and monitoring IQE. Figure 29 shows the results. It can be seen that while the doping peak is located very near the surface, there is almost no change in the IQE. However, when the dopants are deeper, IQE starts to drop. Drop of several percent is observed when the peak is deeper than 0.4 μm. Furthermore, it seems that the light wavelength does not matter because the change in IQE is approximately equally large with all wavelengths. This was expected because the losses are related to the current collection mechanism which affects identically all photogenerated carriers, regardless of their origin.

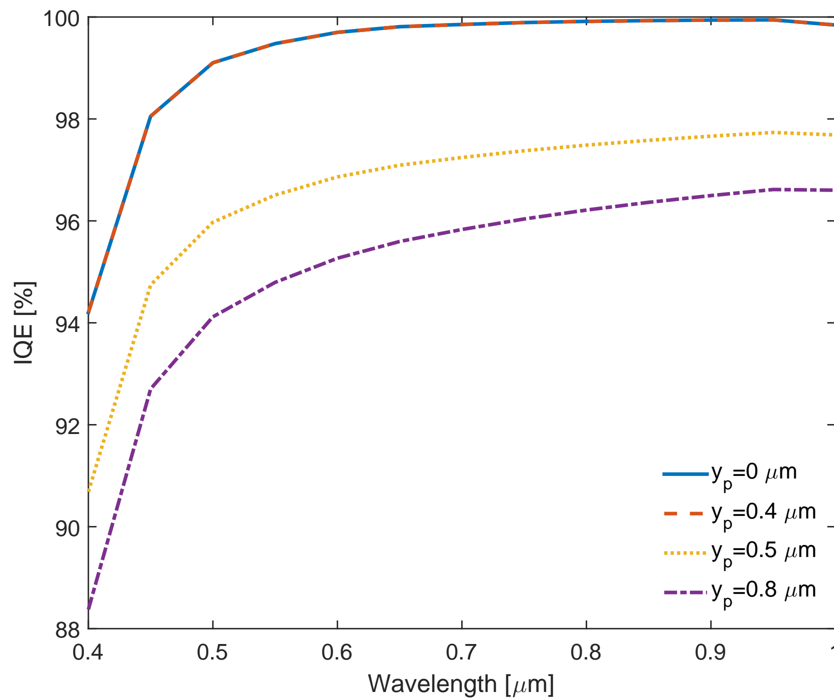

Figure 29: IQE as a function of light wavelength with different contact doping depths. y_p indicates how deep below metal the doping concentration peak is located.

The drop in IQE can be explained by pn-junction theory. Since the substrate is n-type and the contact doping is p-type, they will form a pn-junction. If the

dopants are too deep below the metal, an n-p-n structure is formed. Consequently, depletion regions will be formed to both sides of the p-layer. As a result the contact is no longer fully ohmic which leads into current losses. To ensure proper ohmic contact, the dopants should be located as close to the surface as possible. According to process simulations made with ICECREM during device fabrication, the peak concentration should be located approximately 0.2 μm below the metal. Thus, this phenomenon should not be responsible for the reduction of IQE observed in the measured response.

Changing the shape of the doping profile was tested next. The peak was kept at the surface but the width of the peak was varied and the resulting IQE was inspected. This study revealed that the width of the peak is not very significant. Differences in the IQE were in the range of parts per million (ppm). Based on these simulations it seems that the doping profile does not have a large impact as long as the dopants are close enough to the metal.

Last experiment related to the contacts was to vary the width of the front contact. In the original design the width was 50 μm and the simulations were used to investigate how narrower or wider contacts change the IQE. The result showed that the change is in ppm range and thus the width is not a very important parameter. One explanation is a phenomenon called current crowding [49]. When current travels parallel to the surface, most of it is collected on the edges of the contacts and the amount of current traversing further will decrease exponentially. The length where $1/e$ of the current gets collected is called transfer length and it is mostly determined by doping concentration. With heavy doping the transfer length is short which means that even narrow contacts are enough for current collection. Consequently, as long as the contacts are wider than the transfer length, the width has insignificant effect on the device performance. However, in reality there are some practical aspects that need to be considered. For example, reliable fabrication of narrow contacts might be challenging. Furthermore, contacting the device into external circuitry might be difficult if the contacts are very narrow. On the other hand, narrow contacts decrease the size of the device which increases the number of devices that can be included on one wafer.

4.2.5 Effects of guard ring

The largest problem in the fabricated photodiodes is that the leakage current is huge compared to typical commercial devices. Leakage current was measured from several fabricated device and it varied between 35 - 1400 nA with reverse bias of 2 V. In commercial devices the leakage current typically ranges from tens to hundreds of picoamperes depending on the size and type of the device [43]. Simulated leakage current with 1 V reverse bias was 1.6 nA/μm. Since a 2D model was used in the simulations, the unit is A/μm. Assuming a square 5 mm$\times$5 mm device chip, the corresponding leakage current is 8 μA which larger than what was measured but still comparable. The difference most likely results from the SRV applied to the chip edges in the simulations. Due to lack of measurement data it was just set to a value that resulted into significant leakage current.

As was already discussed in section 2.1, adding a guard ring around the photodiode should significantly decrease the leakage current. Simulations were performed to proof this claim. The simulated structure was identical to figure 14 except additional electrodes were added to the left and right sides of the device. The gap between the guard ring and anode was a parameter that was varied between simulations. If the Al_2O_3 is left on top of this gap, the inversion layer still exists along the gap which could allow some current to bypass the guard ring. Thus, removing inversion from the gap by removing the alumina should even further decrease the leakage current. This was tested by performing the same simulations with and without the oxide on the gap and inspecting the resulting leakage current.

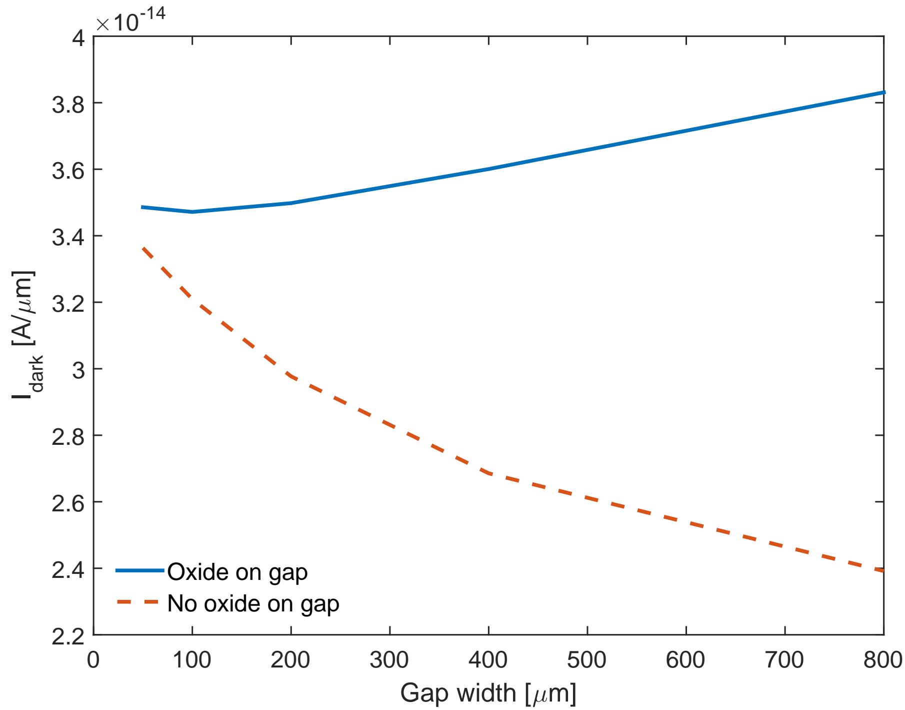

Figure 30: Simulated leakage currents with different gap widths between anode and guard ring. Separate curves are shown for cases with and without oxide on the gap.

The results of the simulations are illustrated in figure 30. It shows the leakage current as a function of the gap width, with and without the oxide on gap. It can be seen that in all cases the leakage current is about five orders of magnitude smaller compared to the device without guard ring. It seems that removing the oxide from the gap further decreases the leakage current. Additionally, increasing the gap width seems to lead to smaller leakage current. Without inversion in the gap, it is difficult for any current that bypasses the guard ring to propagate to the anode. When the oxide is left on the gap, wider gap translates into larger leakage current. Since the inversion exist in the gap, any current created on the gap surface can reach the anode. Thus, a narrow gap translates into a smaller leakage current. As a conclusion, it seems that the best result is obtained if the oxide is removed from the gap and

the gap width is maximized. However, increasing the gap size will also increase the total size of the device. To maximize the number of chips on a wafer this might not be wanted in commercial devices and thus a compromise between device size and leakage current has to be made.

5 Conclusions

Extensive device simulations of induced junction black silicon photodiodes were performed with Silvaco Atlas. The photodiode is based on a new concept which utilizes inversion layer in very lightly doped silicon for carrier collection and b-Si for eliminating optical reflections. Combination of these two properties lead into devices performance very close to ideal. Based on the findings from simulations, an improved version of the photodiode was designed.

The simulation results confirmed several speculations and in general they are in agreement with the theory. The simulations suggested that negatively charged conformal Al_2O_3 film deposited on top of b-Si effectively repels almost all electrons away from the spikes. Together with the excellent chemical passivation resulting from conformal ALD deposition, this result explains the impressive surface passivation observed experimentally. Furthermore, the results showed that the electric field under b-Si becomes flat very quickly which suggests that the bulk electric field should be similar than in planar photodiodes. Since electrons are the majority charge carriers in the substrate, the absence of holes near the surface indicates that a strong inversion layer is induced and according to simulations, it leads into formation of approximately 30 μm deep depletion region. The sheet resistance of the inversion layer was found to decrease linearly as a function of increasing oxide charge. Sharp features in the geometry of b-Si enhance the electric field resulting into approximately seven times larger effective oxide charge compared to planar surface. As a result the inversion layer sheet resistance should be lower in b-Si than in planar. Simulation results indicate that it should be even low enough so that the same concept could be utilized in solar cells.

Simulations concerning the operation of the device revealed that applying reverse bias widens the depletion region similarly than in traditional photodiodes. The resulting behavior of depletion width and capacitance is in excellent agreement with analytic calculations. The simulated spectral response of the photodiode was similar to the measured one but with couple of differences. With wavelengths longer than 400 nm, the measured IQE was several percent below 100 % but the simulations suggest that the IQE should even exceed 99 %. The exact reason for the difference was not identified in the simulations. Either there is still some phenomenon that is not included in the simulations or the losses result from unidealities in the fabrication or measurement preparation steps. For example, during sample preparation before measuring the spectral response, the devices were exposed to unclean air and thus some particles may have landed on the active area of the devices. Furthermore, it was not possible to prepare the samples without touching the front side of the devices which could have caused small scratches or other damage. Since the response was measured by illuminating the whole active area, these< possible small damaged areas caused by device handling could easily cause a deviation of a few percent in the response.

Simulating short wavelength operation turned out to be challenging. First of all, it was not possible to obtain adequate mesh density near the surface which lead into severe errors with wavelengths shorter than 400 nm. Secondly, measurements suggest

that IQE should be over 100 % with short wavelengths due to secondary ionization. However, significant secondary ionization could not be produced with the simulator. Despite these problems, at least the longer wavelength simulations should be reliable.

Investigation of how different parameters affect the spectral response revealed some interesting facts. The results suggest that larger oxide charge density results into higher IQE with all wavelengths but the difference is negligibly small with low light intensities. However, the oxide charge becomes more important with higher intensities because of the stronger inversion. Consequently, a high IQE could be maintained with larger light intensities when a larger oxide charge was applied. Doping concentration of the substrate turned out to have a larger contribution when no bias is applied. Higher dopant concentration results into narrower depletion region which decreases IQE several percent with long wavelengths. Contact width or doping profile seem to cause almost no change into IQE as long as the contact is ohmic. If the dopants are driven too deep below the metal, a decrease of several percent with all wavelengths was detected.

In the first version of the photodiode, high leakage current was the largest problem. Implementing a guard ring structure around the photodiode should significantly improve the situation. Simulations supported this hypothesis. Five orders of magnitude decrease in the leakage current was observed. Based on the findings, a new device with a guard ring was designed. Unfortunately, the fabrication process took so long time that measurement results from the new batch could not be included in this thesis.

Obviously, the next step after this work is to test and characterize the new detectors and compare the results with simulations. Next step after that is to further develop the device for practical applications. For example, the plan is to test if the photodiode could be utilized in a computed tomography scanner. If the results are promising the ultimate goal is to develop a commercial product out of the photodiode. Another option for further research is to test if the same black silicon induced junction concept works in solar cells as well.

References

[1] P. B. Clapham and M. C. Hutley, “Reduction of lens reflexion by the "Moth Eye" principle,” *Nature*, vol. 244, pp. 281–282, 1973.

[2] P. Repo, A. Haarahiltunen, L. Sainiemi, M. Yli-Koski, H. Talvitie, M. C. Schubert, and H. Savin, “Effective passivation of black silicon surfaces by atomic layer deposition,” *Photovoltaics, IEEE Journal of*, vol. 3, no. 1, pp. 90–94, 2013.

[3] G. von Gastrow, R. Alcubilla, P. Ortega, M. Yli-Koski, S. Conesa-Boj, A. F. i Morral, and H. Savin, “Analysis of the atomic layer deposited Al_2O_3 field-effect passivation in black silicon,” *Solar Energy Materials and Solar Cells*, vol. 142, pp. 29 – 33, 2015, proceedings of the 5th International Conference on Crystalline Silicon Photovoltaics (SiliconPV 2015). [Online]. Available: http://www.sciencedirect.com/science/article/pii/S0927024815002329

[4] H. Savin, P. Repo, G. von Gastrow, P. Ortega, E. Calle, M. Garín, and R. Alcubilla, “Black silicon solar cells with interdigitated back-contacts achieve 22.1% efficiency,” *Nature nanotechnology*, 2015.

[5] D. C. Valluru, “Surface passivated black silicon photodetectors with induced junction,” Master’s thesis, Aalto University, 2015.

[6] T. E. Hansen, “Silicon UV-photodiodes using natural inversion layers,” *Physica Scripta*, vol. 18, no. 6, p. 471, 1978. [Online]. Available: http://stacks.iop.org/1402-4896/18/i=6/a=025

[7] I. Müller, U. Johannsen, U. Linke, L. Socaciu-Siebert, M. Smîd, G. Porrovecchio, M. Sildoja, F. Manoocheri, E. Ikonen, J. Gran, T. Kübarsepp, G. Brida, and L. Werner, “Predictable quantum efficient detector: II. characterization and confirmed responsivity,” *Metrologia*, vol. 50, no. 4, p. 395, 2013. [Online]. Available: http://stacks.iop.org/0026-1394/50/i=4/a=395

[8] M. U. Pralle, J. E. Carey, H. Haddad, C. Vineis, J. Sickler, X. Li, J. Jiang, F. Sahebi, C. Palsule, and J. McKee, “IR CMOS: infrared enhanced silicon imaging,” *Proc. SPIE*, vol. 8704, pp. 870 407–870 407–7, 2013. [Online]. Available: http://dx.doi.org/10.1117/12.2015959

[9] M. J. Yaffe and J. A. Rowlands, “X-ray detectors for digital radiography,” *Physics in Medicine and Biology*, vol. 42, no. 1, p. 1, 1997. [Online]. Available: http://stacks.iop.org/0031-9155/42/i=1/a=001

[10] H. Zhang, C. H. Chon, X. Pan, and D. Li, “Methods for counting particles in microfluidic applications,” *Microfluidics and Nanofluidics*, vol. 7, no. 6, pp. 739–749, 2009. [Online]. Available: http://dx.doi.org/10.1007/s10404-009-0493-7

[11] K. Hane, T. Endo, Y. Ito, and M. Sasaki, “A compact optical encoder with micromachined photodetector,” *Journal of Optics A: Pure*

and Applied Optics, vol. 3, no. 3, p. 191, 2001. [Online]. Available: http://stacks.iop.org/1464-4258/3/i=3/a=307

[12] P. Büchele, M. Richter, S. F. Tedde, G. J. Matt, G. N. Ankah, R. Fischer, M. Biele, W. Metzger, S. Lilliu, O. Bikondoa *et al.*, "X-ray imaging with scintillator-sensitized hybrid organic photodetectors," *Nature Photonics*, 2015.

[13] M. Juntunen, "Development of tileable silicon photodiodes for X-ray imaging," Ph.D. dissertation, Aalto University, 2013.

[14] C. C. Hu, *Modern Semiconductor Devices for Integrated Circuits.* Pearson Education, 2010.

[15] S. M. Sze and K. K. Ng, *Physics of Semiconductor Devices*, 3rd ed. John Wiley & Sons, 2007.

[16] J. S. Wilson, *Sensor technology handbook.* Elsevier Science & Technology, 2005.

[17] M. J. Deen and P. K. Basu, *Silicon photonics : fundamentals and devices.* John Wiley & Sons, 2012.

[18] M. A. Green, "Self-consistent optical parameters of intrinsic silicon at 300 K including temperature coefficients," *Solar Energy Materials and Solar Cells*, vol. 92, no. 11, pp. 1305 – 1310, 2008. [Online]. Available: http://www.sciencedirect.com/science/article/pii/S0927024808002158

[19] E. S. Yang, *Fundamentals of Semiconductor Devices.* McGraw-Hill, 1978.

[20] H. Haug, "New methods for investigation of surface passivation layers for crystalline silicon solar cells," Ph.D. dissertation, University of Oslo, 2014.

[21] W. Shockley and W. T. Read, "Statistics of the recombinations of holes and electrons," *Phys. Rev.*, vol. 87, pp. 835–842, Sep 1952. [Online]. Available: http://link.aps.org/doi/10.1103/PhysRev.87.835

[22] R. N. Hall, "Electron-hole recombination in germanium," *Physical Review*, vol. 87, no. 2, p. 387, 1952.

[23] D. Roulston, N. Arora, and S. G. Chamberlain, "Modeling and measurement of minority-carrier lifetime versus doping in diffused layers of n+-p silicon diodes," *Electron Devices, IEEE Transactions on*, vol. 29, no. 2, pp. 284–291, Feb 1982.

[24] A. Richter, S. W. Glunz, F. Werner, J. Schmidt, and A. Cuevas, "Improved quantitative description of auger recombination in crystalline silicon," *Phys. Rev. B*, vol. 86, p. 165202, Oct 2012. [Online]. Available: http://link.aps.org/doi/10.1103/PhysRevB.86.165202

[25] J. Dziewior and W. Schmid, "Auger coefficients for highly doped and highly excited silicon," *Applied Physics Letters*, vol. 31, no. 5, pp. 346–348, 1977. [Online]. Available: http://scitation.aip.org/content/aip/journal/apl/31/5/10.1063/1.89694

[26] A. B. Sproul, “Dimensionless solution of the equation describing the effect of surface recombination on carrier decay in semiconductors,” *Journal of Applied Physics*, vol. 76, no. 5, pp. 2851–2854, 1994. [Online]. Available: http://scitation.aip.org/content/aip/journal/jap/76/5/10.1063/1.357521

[27] A. G. Aberle, “Surface passivation of crystalline silicon solar cells: a review,” *Progress in Photovoltaics: Research and Applications*, vol. 8, no. 5, pp. 473–487, 2000. [Online]. Available: http://dx.doi.org/10.1002/1099-159X(200009/10)8:5<473::AID-PIP337>3.0.CO;2-D

[28] M. S. Bazilchuk, “Improved induced diode photodetectors by increased fixed charge in PECVD amorphous silicon nitride,” Master’s thesis, Norwegian University of Science and Technology, 2014.

[29] S. Kolodinski, J. H. Werner, T. Wittchen, and H. J. Queisser, “Quantum efficiencies exceeding unity due to impact ionization in silicon solar cells,” *Applied Physics Letters*, vol. 63, no. 17, pp. 2405–2407, 1993. [Online]. Available: http://scitation.aip.org/content/aip/journal/apl/63/17/10.1063/1.110489

[30] O. Christensen, “Quantum efficiency of the internal photoelectric effect in silicon and germanium,” *Journal of Applied Physics*, vol. 47, no. 2, pp. 689–695, 1976. [Online]. Available: http://scitation.aip.org/content/aip/journal/jap/47/2/10.1063/1.322635

[31] F. J. Wilkinson, A. J. D. Farmer, and J. Geist, “The near ultraviolet quantum yield of silicon,” *Journal of Applied Physics*, vol. 54, no. 2, pp. 1172–1174, 1983. [Online]. Available: http://scitation.aip.org/content/aip/journal/jap/54/2/10.1063/1.332095

[32] D. K. Schroder, *Semiconductor Material and Device Characterization*, 2nd ed. John Wiley & Sons, 1998.

[33] B. E. Deal, M. Sklar, A. Grove, and E. Snow, “Characteristics of the surface-state charge (Qss) of thermally oxidized silicon,” *Journal of the Electrochemical Society*, vol. 114, no. 3, pp. 266–274, 1967.

[34] M. M. Sildoja, F. Manoocheri, M. Merimaa, E. Ikonen, I. Müller, L. Werner, J. Gran, T. Kübarsepp, M. Smîd, and M. L. Rastello, “Predictable quantum efficient detector: I. photodiodes and predicted responsivity,” *Metrologia*, vol. 50, no. 4, p. 385, 2013. [Online]. Available: http://stacks.iop.org/0026-1394/50/i=4/a=385

[35] G. Dingemans and W. Kessels, “Status and prospects of Al_2O_3-based surface passivation schemes for silicon solar cells,” *Journal of Vacuum Science & Technology A*, vol. 30, no. 4, p. 040802, 2012.

[36] A. J. Bett, J. Eisenlohr, O. Höhn, P. Repo, H. Savin, B. Bläsi, and J. C. Goldschmidt, “Wave optical simulation of the light trapping properties of black

silicon surface textures," *Opt. Express*, vol. 24, no. 6, pp. A434–A445, Mar 2016. [Online]. Available: http://www.opticsexpress.org/abstract.cfm?URI=oe-24-6-A434

[37] J. Oh, H.-C. Yuan, and H. M. Branz, "An 18.2%-efficient black-silicon solar cell achieved through control of carrier recombination in nanostructures," *Nature nanotechnology*, vol. 7, no. 11, pp. 743–748, 2012.

[38] E. Garnett and P. Yang, "Light trapping in silicon nanowire solar cells," *Nano letters*, vol. 10, no. 3, pp. 1082–1087, 2010.

[39] J. Zhu, Z. Yu, G. F. Burkhard, C.-M. Hsu, S. T. Connor, Y. Xu, Q. Wang, M. McGehee, S. Fan, and Y. Cui, "Optical absorption enhancement in amorphous silicon nanowire and nanocone arrays," *Nano Letters*, vol. 9, no. 1, pp. 279–282, 2009, pMID: 19072061. [Online]. Available: http://dx.doi.org/10.1021/nl802886y

[40] T.-H. Her, R. J. Finlay, C. Wu, S. Deliwala, and E. Mazur, "Microstructuring of silicon with femtosecond laser pulses," *Applied Physics Letters*, vol. 73, no. 12, pp. 1673–1675, 1998. [Online]. Available: http://scitation.aip.org/content/aip/journal/apl/73/12/10.1063/1.122241

[41] L. Sainiemi, V. Jokinen, A. Shah, M. Shpak, S. Aura, P. Suvanto, and S. Franssila, "Non-reflecting silicon and polymer surfaces by plasma etching and replication," *Advanced Materials*, vol. 23, no. 1, pp. 122–126, 2011. [Online]. Available: http://dx.doi.org/10.1002/adma.201001810

[42] S. Jeong, M. D. McGehee, and Y. Cui, "All-back-contact ultra-thin silicon nanocone solar cells with 13.7% power conversion efficiency," *Nature communications*, vol. 4, 2013.

[43] *Si Photodiodes: Lineup of Si photodiodes for UV to near IR, radiation*, Hamamatsu photonics, 2014. [Online]. Available: https://www.hamamatsu.com/resources/pdf/ssd/si_pd_kspd0001e.pdf

[44] E. Mazur, "Laser doping and texturing of silicon for advanced optoelectronic devices," in *11th Conference on Lasers and Electro- Optics Pacific Rim (CLEO-PR)*, 2015.

[45] M. Aurientis, "Interdigitated back contact n-type solar cell with black silicon anti-reflecting layer: Simulations and experiments," Master's thesis, Aalto University, 2014.

[46] *Atlas user's manual*, Silvaco, inc, September 2015. [Online]. Available: https://dynamic.silvaco.com/dynamicweb/jsp/downloads/DownloadManualsAction.do?req=silentmanuals&nm=atlas

[47] S. Franssila, *Introduction to Microfabrication*, 2nd ed. John Wiley & Sons, 2010.

[48] F. Werner, Y. Larionova, D. Zielke, T. Ohrdes, and J. Schmidt, "Aluminum-oxide-based inversion layer solar cells on n-type crystalline silicon: Fundamental properties and efficiency potential," *Journal of Applied Physics*, vol. 115, no. 7, 2014. [Online]. Available: http://scitation.aip.org/content/aip/journal/jap/115/7/10.1063/1.4865962

[49] H. Murrmann and D. Widmann, "Current crowding on metal contacts to planar devices," *IEEE Transactions on Electron Devices*, vol. 16, no. 12, pp. 1022–1024, Dec 1969.